NONLINEAR DYNAMICS OF A CYLINDER IN STEADY AXIAL FLOW

J.L. LOPES M.P. PAÏDOUSSIS C. SEMLER

M.E.R.L. Report 99-2

June 1999

Department of Mechanical Engineering, McGill University

Montreal, Québec, Canada, H3A 2K6

TABLE OF CONTENTS

1.	II	NTRO	ODUCTION	4
2.	Е	QUA	TIONS OF MOTION	5
3.	N	1ETH	IODS OF SOLUTION	8
2	3.1	CAI	NTILEVERED CYLINDERS	8
2	3.2	CYI	LINDERS FIXED AT BOTH ENDS 1	0
4.	L	INEA	AR DYNAMICS 1	2
4	4.1	DY	NAMICAL BEHAVIOUR OF INEXTENSIBLE AND EXTENSIBLE	
(CAI	NTIL	EVERED CYLINDERS1	2
4	4.2	EFF	FECTS OF SOME SYSTEM PARAMETERS ON STABILITY OF	
(CAI	NTIL	EVERED CYLINDERS1	4
	4.	.2.1	Effect of f on stability	4
	4.	.2.2	Effects of εc_N , εc_T and f on stability	6
	4.	.2.3	Effects of β and f on stability	9
5.	N	ONL	INEAR DYNAMICS2	0
	5.1	NUI	MERICAL METHODS2	0
	5.2	NO	NLINEAR DYNAMICAL BEHAVIOUR OF CANTILEVERED CYLINDERS 2	1
	5	.2.1	Comparison with an experience	1
	5	.2.2	Further discussions	5
6.	C	ONC	CLUSION	7
TA	BL	ES	3	0
EI/	~T II	DEC	2	1

APPENDIX A	48
APPENDIX B	69
APPENDIX C	71
APPENDIX D	74
APPENDIX E	75

Here, after recalling the expression of the dimensionless equations of motion of the cantilevered cylinder in the inextensible and extensible cases, the equations are discretized via Ritz-Galerkin procedure. Typical results by linear analysis show that the system loses stability by divergence in the first mode, and then by flutter in the second and higher modes. Variations of the critical flow velocity for onset of divergence (buckling) and flutter through a Hopf bifurcation show that decreasing the slenderness parameter f and increasing the normal viscous parameter ϵc_N stabilizes the system. Nonlinear bifurcation diagrams show that, typically, the system is restabilized after divergence and, after that, flutter develops with increasing, then decreasing amplitude with increasing flow velocity; a secondary bifurcation then leads to flutter in a higher mode. Near this secondary bifurcation, interesting dynamics may be observed, namely quasiperiodicity, and over a narrow-flow range, weak chaos.

1. INTRODUCTION

Slender cylinders in axial flow are found in certain regions of heat exchangers in the form of clusters of tubes, as reactivity-monitoring and control rods or as clustered fuel-element bundles in nuclear reactors, as towed bags for fresh-water and oil transport by sea, in-flight refuelling lines for aircraft, towed arrays of very long cylinders equipped with hydrophones for oil exploration, and many other applications.

All the theoretical work on this topic has been based on linear theory. Hence, such important issues as transition from one linear instability mode to another cannot truly be addressed (if in fact it occurs at all), limit-cycle amplitudes, and the rest of the rich kaleidoscope

of dynamical behaviour that may be revealed by nonlinear theory. This situation is being partly redressed for the first time by this first attempt to study the nonlinear dynamics of the system.

Based on the equations of motion derived and presented in detail in Lopes *et al.* [1] for the inextensible and extensible cantilevered cylinder immersed in axial flow, the methods of solution are briefly reviewed (Section 3); then, some classical linear analysis is undertaken in order to study the stability of the system and to investigate the effects of the variation of some parameters on the stability, namely the slenderness parameter f, the viscous parameter f and the mass ratio parameter f (Section 4); finally, nonlinear analysis is conducted by means of bifurcation, phase-plane, and time versus flow-velocity diagrams, showing amplitudes of the displacement of the tip, as well as transitions from one mode to another.

2. EQUATIONS OF MOTION

The system under consideration consists of a cylinder of length L, cross-sectional area A, mass per unit length m and flexural rigidity EI, contained in a rigid channel within which a fluid of density ρ flows with mean flow velocity U parallel to the channel centreline and to the position of rest of the cylinder. The cylinder is assumed to initially lie along the X-axis (in the direction of gravity, coincident with the channel centreline) and to oscillate in the (X,Y) plane. The system can be either cantilevered or supported at both ends. When the cylinder is cantilevered, it is assumed to be terminated by a tapering end, the cross-sectional area of which varies smoothly from S to 0 in a distance l, where $l/L \ll 1$. The equations of motion have been derived using Hamilton's principle by Lopes $et\ al$. [1].

For a cantilevered cylinder, the equation of motion may be written in nondimensional form as follows:

$$\begin{split} &\left(1+(\chi-1)\beta\right)\ddot{\eta}+2\mathcal{U}\sqrt{\beta}\chi\,\dot{\eta}'\left(1+\frac{7}{4}\eta'^2\right)+\mathcal{U}^2\chi\,\eta''\left(1+\frac{5}{2}\eta'^2\right)-\frac{3}{2}\chi\,\dot{\eta}\eta'\left(\beta\,\dot{\eta}'+\mathcal{U}\sqrt{\beta}\,\eta''\right)\\ &+\left(\frac{1}{2}\,\mathcal{U}^2\varepsilon\,c_f+\gamma_c\right)\left(\eta'+\frac{1}{2}\eta'^3-(1-\xi)\left(\eta''+\frac{3}{2}\eta'^2\eta''\right)\right)-\frac{1}{2}\,\mathcal{U}^2\,c_b\left(\eta''+\frac{3}{2}\eta'^2\eta''\right)\\ &+\left(\frac{1}{2}\,\mathcal{U}^2\varepsilon\,c_fh-\gamma_F\right)\left(\eta'+\eta'^3-(1-\xi)\left(\eta''+\frac{3}{2}\eta'^2\eta''\right)\right)+\eta''''+4\eta'\eta''\eta'''+\eta''^3+\eta''''\eta'^2\\ &+\frac{1}{2}\,\mathcal{U}^2\varepsilon\left[c_f\left(\frac{\sqrt{\beta}}{\mathcal{U}}\dot{\eta}-\frac{1}{2}\frac{\beta}{\mathcal{U}^2}\dot{\eta}^2\eta'-\frac{1}{2}\frac{\sqrt{\beta}}{\mathcal{U}}\dot{\eta}\eta'^2-\frac{1}{2}\frac{\beta^{3/2}}{\mathcal{U}^3}\dot{\eta}^3\right)+c_d\left(\eta'|\eta'|+\frac{\sqrt{\beta}}{\mathcal{U}}\left(\dot{\eta}|\eta'|+\eta'|\dot{\eta}|\right)+\frac{\beta}{\mathcal{U}^2}\dot{\eta}|\dot{\eta}|\right)\right]\\ &-\eta''(1-\beta)\int_{\xi}^{\xi}\int_{0}^{\xi}(\dot{\eta}'^2+\eta'\ddot{\eta}')\,d\xi\,d\xi-\chi\,\eta''\int_{\xi}^{\xi}(\beta\,\ddot{\eta}\eta'+2\mathcal{U}\sqrt{\beta}\,\dot{\eta}'\eta'+\mathcal{U}^2\eta''\eta')\,d\xi\\ &+\eta'\left(1+(\chi-1)\beta\right)\int_{0}^{\xi}(\dot{\eta}'^2+\eta'\ddot{\eta}')\,d\xi+2\chi\left(\beta\,\dot{\eta}'+\mathcal{U}\sqrt{\beta}\,\eta''\right)\int_{0}^{\xi}\eta'\dot{\eta}'\,d\xi-\frac{1}{2}\varepsilon\,c_f\beta\,\dot{\eta}\int_{0}^{\xi}\eta'\dot{\eta}'\,d\xi\\ &-\eta''\int_{\xi}^{\xi}\left[\left(\frac{1}{2}\,\mathcal{U}^2\varepsilon\,c_fh-\gamma_F\right)\left(\frac{1}{2}\eta'^2-(1-\xi)\eta'\eta''\right)-\frac{1}{2}\,\mathcal{U}^2\,c_b\,\eta'\eta''-\frac{1}{4}\varepsilon\,c_f\beta\,\dot{\eta}^2\right]d\xi+\mathcal{O}(\mathcal{M})=0. \end{split}$$

where $\eta(\xi,\tau)$ represents the lateral deflection of the cylinder. Dots and primes denote respectively derivatives with respect to the nondimensional time, τ , and the nondimensional curvilinear co-ordinate along the centreline of the cylinder, ξ . The nondimensional parameters in (1) are defined by

$$\xi = \frac{s}{L}, \quad \eta = \frac{y}{L}, \quad \tau = \left(\frac{EI}{m + \rho A}\right)^{1/2} \frac{t}{L^2}, \quad \mathcal{U} = \left(\frac{\rho A}{EI}\right)^{1/2} UL, \quad \beta = \frac{\rho A}{m + \rho A}, \quad \gamma_F = \frac{\rho g A L^3}{EI},$$

$$\gamma_C = \frac{mgL^3}{EI}, \quad c_f = \frac{4}{\pi} C_f, \quad c_d = \frac{4}{\pi} C_{DP}, \quad c_b = \frac{4}{\pi} C_b, \quad \varepsilon = \frac{L}{D}, \quad h = \frac{D}{D_h},$$

(2)

where s is the curvilinear co-ordinate along the cylinder, C_f is a frictional coefficient associated with the mean flow over the cylinder, C_{DP} is a frictional coefficient for motions in stagnant fluid and D_h is the hydraulic diameter. [Note that the frictional coefficient C_f might be replaced by

 C_N and C_T , the coefficients associated with friction in the normal and tangential directions respectively, and in general not equal (refer to [1])].

For a cylinder fixed at both ends, the motion is governed by the following two nondimensional equations:

$$\begin{split} &(1-\beta)\ddot{u}-\chi\left(\beta\ddot{v}v'+2\mathcal{U}\sqrt{\beta}\ddot{v}v'v'+\mathcal{U}^{2}v''v'\right)-\Pi_{0}u''-\Pi_{0}v'v''-v''v'''-v'v''''\\ &-\left(\frac{1}{2}\mathcal{U}^{2}\varepsilon\,c_{f}(1+h)+\gamma_{c}-\gamma_{F}\right)\left(\frac{1}{2}v'^{2}-(1-\xi)\,v'v''\right)+(\Gamma+\Pi)v'v''+\frac{1}{4}\varepsilon\,c_{f}\beta\dot{v}^{2}\\ &-\frac{1}{2}\mathcal{U}^{2}\varepsilon\,c_{d}v'\left(v'|v'|+\frac{\sqrt{\beta}}{\mathcal{U}}\left(v'|\dot{v}|+\dot{v}|v'|\right)+\frac{\beta}{\mathcal{U}^{2}}\dot{v}|\dot{v}|\right)+\delta\left(-\frac{1}{2}\left(\frac{1}{2}\mathcal{U}^{2}\varepsilon\,c_{f}+\gamma_{c}\right)+\overline{\Gamma}-\Gamma\right)v'v''+\mathcal{O}(\tilde{\mathcal{M}})=0,\\ &(3)\\ &(1+(\chi-1)\beta)\ddot{v}+2\mathcal{U}\sqrt{\beta}\,\chi\dot{v}'\left(1-\frac{7}{4}v'^{2}\right)+\mathcal{U}^{2}\chi\,v''\left(1-\frac{5}{2}v'^{2}\right)-\chi\,v'\left(\beta\ddot{u}+3\,\mathcal{U}\sqrt{\beta}\,\dot{u}'+2\mathcal{U}^{2}\,u''\right)\\ &-\chi\beta\ddot{v}v'^{2}-\chi\left(4\mathcal{U}u'+2\sqrt{\beta}\,\dot{u}+\frac{3}{2}\sqrt{\beta}\,\dot{v}v'\right)\left(\sqrt{\beta}\,\dot{v}'+\mathcal{U}v''\right)+\left(\frac{1}{2}\mathcal{U}^{2}\varepsilon\,c_{f}h-\gamma_{F}\right)\left(v'-2u'v'-\frac{1}{2}v'^{3}\right)\\ &+\left(\frac{1}{2}\mathcal{U}^{2}\varepsilon\,c_{f}+\gamma_{c}\right)\left(v'-u'v'-\frac{1}{2}v'^{3}\right)+\left(\Gamma+\left(\frac{1}{2}\mathcal{U}^{2}\varepsilon\,c_{f}+\gamma_{c}\right)\left(1-\xi\right)\right)\left(-v''+u''v'+\frac{3}{2}v'^{2}v''\right)\\ &+v''''-\left(3u'''v''+4u''v'''+2u'v''''+2v'''+2v'''+8v'v''v'''\right)-\Pi_{0}\left(u''v'+u'v''+\frac{3}{2}v'^{2}v''\right)\\ &+\left(\Pi+\left(\frac{1}{2}\mathcal{U}^{2}\varepsilon\,c_{f}h-\gamma_{F}\right)\left(1-\xi\right)\right)\left(-v''+u''v'+2u'v''+\frac{3}{2}v'^{2}v''\right)\\ &+\delta\left(-\frac{1}{2}\left(\frac{1}{2}\mathcal{U}^{2}\varepsilon\,c_{f}+\gamma_{c}\right)+\overline{\Gamma}-\Gamma\right)\left(-v''+u''v'+u'v''+\frac{3}{2}v'^{2}v''\right)\\ &+\frac{1}{2}\mathcal{U}^{2}\varepsilon\,c_{f}\left(\frac{\sqrt{\beta}}{\mathcal{U}}\dot{v}+\frac{\beta}{\mathcal{U}}u'\dot{v}+\frac{\beta}{\mathcal{U}^{2}}\dot{u}\dot{v}^{3}\right)+\frac{1}{2}\mathcal{U}^{2}\varepsilon\,c_{d}\left(v'|v'|+\frac{\sqrt{\beta}}{\mathcal{U}}\left(v'|\dot{v}|+\dot{v}|v'|\right)+\frac{\beta}{\mathcal{U}^{2}}\dot{v}|\dot{v}\right)+\mathcal{O}(\tilde{\mathcal{M}})=0 \end{array}$$

u and v represent the nondimensional longitudinal and transverse displacements respectively, $u = u^* / L$ and $v = v^* / L$, the starred quantities being the dimensional displacements. Here, the prime denotes the derivative with respect to the nondimensional co-ordinate, ξ , with $\xi = X/L$, X being the Lagrangian co-ordinate. In addition to the parameters in equation (2), in this case the

dimensionless tension at the downstream end Γ , the externally imposed uniform tension $\overline{\Gamma}$, and axial flexibility Π_0 , need to be defined,

$$\Gamma = T(L) L^2 / EI, \quad \overline{\Gamma} = \overline{T} L^2 / EI, \quad \Pi_0 = EAL^2 / EI.$$
 (5)

3. METHODS OF SOLUTION

To obtain solutions of the equation of motion, the system is discretized by the Ritz-Galerkin technique, making use of the modal shapes of a freely vibrating beam satisfying the same boundary conditions as the cylinder, as a suitable set of base functions. These latter, satisfying both geometric and natural boundary conditions, are the so-called comparison functions.

3.1 CANTILEVERED CYLINDERS

In the case of a cantilevered cylinder, the boundary conditions at s = 0 are y(0) = y'(0) = 0; furthermore, at s = L, y''(L) = 0. Moreover, a special boundary condition properly accounting for the presence of the tapering-end has been determined [1], namely

$$-EIy''' + \left[fM(\ddot{y} + U\dot{y}') + m\ddot{y} \right] s_e - fMU(\dot{y} + Uy') + (\rho_c - \rho)Agy' s_e$$
$$+ \frac{1}{2} \rho DU^2 C_f hy' s_e + \frac{1}{2} \rho DU C_f (\dot{y} + Uy') \overline{s}_e = 0 \quad \text{at} \quad s = 1,$$

with $s_e = (1/A) \int_{L-l}^{L} A(s) ds$ and $\bar{s}_e = (1/D) \int_{L-l}^{L} D(s) ds$, A being the cross-section area, and where the parameter f is a measure of the departure from ideal slender-body, inviscid flow theory arising from (i) the lateral flow not being truly two-dimensional across the tapered end-piece, and (ii) boundary layer effects [2-3]. Thus, normally $0 \le f \le 1$; for f = 1 we have an ideally streamlined

free end, and for f = 0 a blunt free end. The nondimensional form of the tapering-end boundary condition is

$$-\eta''' + \chi_e \Big[\Big(1 + (\chi f - 1)\beta \Big) \ddot{\eta} + \chi f \mathcal{U} \sqrt{\beta} \dot{\eta}' \Big] + \Big(\frac{1}{2} \overline{\chi}_e \varepsilon c_f - \chi f \Big) \Big(\mathcal{U} \sqrt{\beta} \dot{\eta} + \mathcal{U}^2 \eta' \Big) + \Big(\frac{1}{2} \mathcal{U}^2 \varepsilon c_f h + \gamma_C - \gamma_F \Big) \chi_e \eta' = 0 \quad \text{at} \quad \xi = 1,$$

(6)

where $\chi_e = s_e / L$, and $\overline{\chi}_e = \overline{s}_e / L$.

For simplicity, let us write equation (1) in the form $F(\eta) = 0$, where η is the dimensionless displacement. Then, adding the boundary conditions, the problem can be formulated in the form

$$F(\eta(\xi,\tau)) + \delta(\xi-1)B(\eta(\xi,\tau)) = 0,$$

$$\eta(0,\tau) = \eta'(0,\tau) = 0, \qquad \eta''(1,\tau) = \eta'''(1,\tau) = 0,$$
(7)

(8)

where $B(\eta)$ in (7) represents the term that counterbalances the shear force in the tapering-end boundary condition (6); $\delta(\xi-1)$ is the Dirac delta function. Proceeding in this way, the tapering-end boundary condition is taken into account in the formulation of an expanded boundary value problem. The reader should refer to Appendix A, where an extensive discussion dealing with two methods to account for this boundary condition is given.

Let us write the nondimensional displacement, η , in the form

$$\eta(\xi,\tau) = \sum_{r=1}^{\infty} \phi_r(\xi) q_r(\tau),$$

(9)

where $\phi_r(\xi)$ represents the cantilevered beam eigenfunctions and $q_r(\tau)$ the generalized coordinates. These eigenfunctions satisfy both geometric and natural boundary conditions of the dry cantilevered-cylinder without a tapering-end, and are defined by

$$\phi_r(\xi) = \cosh(\Lambda_r \xi) - \cos(\Lambda_r \xi) - \sigma_r(\sinh(\Lambda_r \xi) - \sin(\Lambda_r \xi)),$$

where the eigenvalues Λ_r satisfy the corresponding characteristic equation, $\cos \Lambda_r \cosh \Lambda_r + 1 = 0; \ \sigma_r = \left[(\cos \Lambda_r + \cosh \Lambda_r) / (\sin \Lambda_r + \sinh \Lambda_r) \right].$

Then, truncating the solution vector (9) to the lowest N terms, substitution of the resulting expression into (1), multiplication by $\phi_i(\xi)$ and integration from 0 to 1 leads to

$$\begin{split} M_{ij}\ddot{q}_{j} + C_{ij}\dot{q}_{j} + K_{ij}q_{j} + r_{ijk}q_{j} &|q_{k}| + \overline{s}_{ijk}|q_{j}|\dot{q}_{k} + \widetilde{s}_{ijk}q_{j}|\dot{q}_{k}| + t_{ijk}\dot{q}_{j}|\dot{q}_{k}| + \alpha_{ijkl}q_{j}q_{k}q_{l} \\ &+ \beta_{ijkl}q_{j}q_{k}\dot{q}_{l} + \gamma_{ijkl}q_{j}\dot{q}_{k}\dot{q}_{l} + \eta_{ijkl}\dot{q}_{j}\dot{q}_{k}\dot{q}_{k} + \mu_{ijkl}q_{j}q_{k}\ddot{q}_{l} = 0, \end{split}$$

(10)

where M_{ij} , C_{ij} , and K_{ij} represent respectively the mass, damping and stiffness matrices, of the linear system. These, as well as α_{ijkl} , β_{ijkl} , γ_{ijkl} , η_{ijkl} , μ_{ijkl} , r_{ijk} , \bar{s}_{ijk} , \bar{s}_{ijk} , and t_{ijk} , are defined in Appendix B.

3.2 CYLINDERS FIXED AT BOTH ENDS

In the case of a cylinder fixed at both ends, we need to consider comparison functions, $\psi_r(\xi)$ and $\phi_r(\xi)$, and generalized co-ordinates, $p_r(\tau)$ and $q_r(\tau)$, in the longitudinal and transverse direction. Thus,

$$u(\xi,\tau) = \sum_{r=0}^{\infty} \psi_r(\xi) p_r(\tau),$$

(11)

$$v(\xi,\tau) = \sum_{r=0}^{\infty} \phi_r(\xi) q_r(\tau),$$

(12)

where $\psi_r(\xi) = \sqrt{2} \sin(r\pi\xi)$ and $\phi_r(\xi) = \sqrt{2} \sin(r\pi\xi)$ for a simply supported cylinder, or $\phi_r(\xi) = \left[\cosh(\Lambda_r\xi) - \cos(\Lambda_r\xi) + \sigma_r(\sinh(\Lambda_r\xi) - \sin(\Lambda_r\xi))\right], \text{ for a cylinder clamped at both ends.}$ In the latter case, we have $\sigma_r = \left[(\sin\Lambda_r + \sinh\Lambda_r)/(\cos\Lambda_r - \cosh\Lambda_r)\right], \text{ and the eigenvalues } \Lambda_r$ satisfy the characteristic equation $\cos\Lambda_r \cosh\Lambda_r - 1 = 0$.

Then, again, truncating the solution vectors (11) and (12) at N and M, respectively, substitution of the resulting expressions into (3) and (4), multiplication by $\psi_i(\xi)$ in (3) and by $\phi_i(\xi)$ in (4, and integration from 0 to 1 leads to

$$M_{ij}^{u} \ddot{p}_{j} + K_{ij}^{u} p_{j} + A_{ijk}^{1} q_{j} q_{k} + A_{ijk}^{2} q_{j} \dot{q}_{k} + A_{ijk}^{3} \dot{q}_{j} \dot{q}_{k} + A_{ijk}^{4} q_{j} \ddot{q}_{k} + B_{ijkl}^{1} q_{j} q_{k} |q_{l}| + B_{ijkl}^{2} q_{j} |q_{k}| \dot{q}_{l}$$

$$+ B_{ijkl}^{3} q_{j} q_{k} |\dot{q}_{l}| + B_{ijkl}^{4} q_{j} \dot{q}_{k} |\dot{q}_{l}| = 0,$$

$$(13)$$

$$\begin{split} M_{ij}^{\nu}\ddot{q}_{j} + C_{ij}^{\nu}\dot{q}_{j} + K_{ij}^{\nu}q_{j} + D_{ijk}^{1}p_{j}q_{k} + D_{ijk}^{2}\dot{p}_{j}q_{k} + D_{ijk}^{3}p_{j}\dot{q}_{k} + D_{ijk}^{4}\dot{p}_{j}\dot{q}_{k} + D_{ijk}^{5}\ddot{p}_{j}q_{k} + E_{ijk}^{1}q_{j}\big|q_{k}\big| + E_{ijk}^{2}\big|q_{j}\big|\dot{q}_{k}\big| \\ + E_{ijk}^{3}q_{j}\big|\dot{q}_{k}\big| + E_{ijk}^{4}\dot{q}_{j}\big|\dot{q}_{k}\big| + F_{ijkl}^{1}q_{j}q_{k}q_{l} + F_{ijkl}^{2}q_{j}q_{k}\dot{q}_{l} + F_{ijkl}^{3}q_{j}\dot{q}_{k}\dot{q}_{l} + F_{ijkl}^{4}\dot{q}_{j}\dot{q}_{k}\dot{q}_{l} + F_{ijkl}^{5}q_{j}q_{k}\ddot{q}_{l} = 0. \end{split}$$

$$(14)$$

 M_{ij}^u , and K_{ij}^u represent the mass, and stiffness matrices in the *u*-direction, whereas M_{ij}^v , C_{ij}^v , and K_{ij}^v represent the mass, damping and stiffness matrices in the *v*-direction. These, as

well as A_{ijk}^1 , A_{ijk}^2 , A_{ijk}^3 , A_{ijk}^4 , B_{ijkl}^1 , B_{ijkl}^2 , B_{ijkl}^3 , B_{ijkl}^4 , and D_{ijk}^1 , D_{ijk}^2 , D_{ijk}^3 , D_{ijk}^4 , D_{ijk}^5 , E_{ijk}^1 , E_{ijk}^2 , E_{ijk}^3 , E_{ijk}^4 , E_{ijk}^4 , E_{ijk}^4 , E_{ijkl}^5 , are defined in Appendix C.

4. LINEAR DYNAMICS

4.1 DYNAMICAL BEHAVIOUR OF INEXTENSIBLE AND EXTENSIBLE CANTILEVERED CYLINDERS

Here the effects of purely axial and steady flow on stability of the cantilevered cylinder are discussed. To this end, solutions of the linear part of equation (10) of the form

$$q(\tau) = e^{\lambda \tau}$$

are considered, λ being a complex dimensionless eigenvalue. If the real part of λ is negative, motions are damped, while if $\text{Re}(\lambda) > 0$ motions are amplified, i.e., the system is unstable.

Figure 1 shows the complex eigenvalue λ plotted as an Argand diagram, with the dimensionless flow velocity \mathcal{U} as parameter, for the lowest three modes of an isolated cantilevered cylinder with a fairly well streamlined free end. For this system, the mass ratio $\beta=0.5$, $\varepsilon c_f=1$, $c_d=0$, $\gamma_c=\gamma_F=0$ (horizontal system), the free end is considered to be fairly well streamlined, with f=0.8, $\chi_e=0.01$, $\overline{\chi}_e=0.01$, $c_b=0$, and the outer channel to be large, with $\chi=1$, h=0. Small axial flow velocities generate $\mathrm{Re}(\lambda)<0$, i.e., flow-induced damping; at sufficiently high flow velocities, however, the cylinder first loses stability by divergence (buckling) in its first mode $(\mathrm{Im}(\lambda)=0,\mathrm{Re}(\lambda)>0)$ and then by flutter through a Hopf bifurcation in its second and third modes $(\mathrm{Im}(\lambda)\neq0,\mathrm{Re}(\lambda)>0)$.

These calculations, carried out with an 8-mode discretisation, and for the same parameters as considered in Ref. [3], give the same flow velocities for divergence ($\mathcal{U}_{cd} = 2.06$) and for regaining of stability ($\mathcal{U} = 4.94$), and somewhat higher flutter velocities in the second and third modes ($\mathcal{U} = 5.25$ and 8.45, versus 5.17 and 8.28, respectively); the discrepancies arise from the tapering-end boundary condition being slightly different from that in Ref. [3].

The calculations in this figure were carried out to sufficiently high \mathcal{U} in all three modes to enable one to observe that (i) the loss of stability in the second mode is preceded by regaining of stability in the first mode, and (ii) in analogous manner, the regaining of stability in the second mode occurs at a slightly higher \mathcal{U} ($\mathcal{U}=8.65$) than is necessary for the onset of third-mode flutter. This seems to predict a range of velocity, after the regaining of stability in the first mode and before flutter in the second mode where the system is stable. This will be confirmed by the nonlinear theory for another set of parameters. However, such a phenomenon was observed in previous experiments conducted by Païdoussis.

These results are obtained with the assumption that the cylinder is inextensible. We may also consider the cantilevered cylinder to be extensible, and make use of the equations of motion derived in the case of a cylinder fixed at both ends (equations (13)and (14)), but subject to to them the cantilever boundary conditions (refer to Appendix D for further details concerning the definition of the matrices).

In this case we need to consider motions in both the longitudinal and transverse directions. Since the linear equations are not coupled, the stability of the system can be studied separately in each direction. The parameters correspond to those defined previously.

Considering the linear equation of motion in the longitudinal direction (equation (13)), we

notice that there is no damping matrix, and, moreover, the stiffness matrix is independent of the fluid velocity. Consequently, the eigenvalues are constant and purely imaginary, which leads to a stable motion with undamped longitudinal oscillations. Hence, some damping should be added to the longitudinal equation of motion in order obtain a more physical behaviour.

In the transverse direction (equation (14)), it has been shown in Ref. [1] that neglecting the axial tension Γ at the downstream, and with the requirement $\delta = 0$ for an end free to slide axially, we obtain the same linear equation governing the motion of the cylinder and hence the same dynamics as in the inextensible case, which is indeed reasonable.

4.2 EFFECTS OF SOME SYSTEM PARAMETERS ON STABILITY OF CANTILEVERED CYLINDERS

Here the effects of the slenderness parameter f, the normal and tangential viscosity parameters εc_N and εc_T , and the mass ratio β , are investigated. We also consider the tapering-end shape to be ellipsoidal (refer to [1]) and its length to represent 1% of the total length of the cylinder, i.e., l/L=0.01, this leading to $\chi_e=0.00667$, $\overline{\chi}_e=0.00785$. All the results were obtained using a 4-mode Galerkin approximation.

4.2.1 Effect of f on stability

The dimensionless critical flow velocity for first-mode divergence \mathcal{U}_{cd} is shown in Figure 2. We actually observe the velocities for loss of stability (the lower part of each curve) and for regaining of stability (the upper part). It may be seen that divergence depends strongly on the free end

streamlining parameter. The system seems to be stabilized as the tapering free-end progressively becomes less than ideally streamlined: for f = 0.6, divergence occurs at $\mathcal{U}_{cd} = 3$; and for $f \leq 0.49$, $\mathcal{U}_{cd} > 14$. However, in the range 0.6 < f < 1.0 the effect on the lowest \mathcal{U}_{cd} is not very pronounced: \mathcal{U}_{cd} varies between 3 and 1.8 approximately.

The dimensionless critical flow velocity for flutter \mathcal{U}_{cf} through a Hopf bifurcation is shown in Figure 3. The evolution of \mathcal{U}_{cf} with decreasing f is quite intricate: the curves shown actually represent critical flow velocities for loss, regaining and new loss of stability. To clarify the dynamical behaviour in Figure 3, Argand diagrams for f = 0.1, 0.4, 0.5, and 0.7 are presented in Figure 4(a-d). In these cases, flutter always occurs in stable or restabilized systems; hence, the linear theory is still valid.

For f = 0.7 (Figure 4(a)), starting from a restabilized solution (first-mode restabilization occurs at $\mathcal{U} = 4.63$) second-mode flutter occurs at $\mathcal{U} = 5.48$; then, the system loses stability in the third mode at $\mathcal{U} = 8.56$, before regaining stability in the second mode at $\mathcal{U} = 8.62$; finally, the system loses stability once again in the second mode at $\mathcal{U} = 14.70$ (actually, we observe that the second mode reaches the real axis after the regaining of stability, remains on it for a while, and then, leaves it just before becoming again unstable).

For f = 0.5 (Figure 4(b)), starting from a stable solution third-mode flutter occurs at $\mathcal{U} = 9.17$; (here, first-mode divergence occurs at $\mathcal{U} = 11.23$ and first-mode restabilization at $\mathcal{U} = 12.06$); then, the system regains stability in the third mode at $\mathcal{U} = 15.04$; finally, flutter occurs in the second mode at $\mathcal{U} = 15.18$ (same comments as before), and, again, in the third mode at $\mathcal{U} = 15.24$.

For f = 0.4 (Figure 4(c)), starting from a stable solution third-mode flutter occurs at $\mathcal{U} = 9.77$; then, the system regains stability in the third mode at $\mathcal{U} = 14.77$; finally, flutter occurs in the fourth mode at $\mathcal{U} = 15.47$, and then, in the second mode at $\mathcal{U} = 15.54$.

For f = 0.1 (Figure 4(d)), starting from a stable solution the system loses first stability by third-mode flutter at $\mathcal{U} = 16.37$, and then by second-mode flutter at $\mathcal{U} = 20.59$. (Here, it should be recalled that the modes are identified by continuity of locus as \mathcal{U} is increased from $\mathcal{U} = 0$. In fact, a second mode, say for $\mathcal{U} > 0$ does not necessarily look at all like a second dry-beam mode, but generally contains higher dry-beam components (refer to [4])).

These Argand diagrams make Figure 3 more comprehensible. Here, the main finding perhaps is that with decreasing f the flow velocities for flutter increase sharply (note scale) and discontinuously. However, we shall keep in mind that a four-mode computation does not efficiently apply for velocities higher than 12, in which case using further modes seems appropriate in order to obtain more accurate results.

Collecting the effects of f on divergence and flutter, it is interesting to note that the system may lose stability by flutter first and then by divergence, for some values of the slenderness parameter (e.g. f = 0.5 or less). Hence, depending on the shape of the tapering free-end, we can either obtain instabilities through buckling or flutter first, or even render the system more stable (when decreasing f drastically).

4.2.2 Effects of εc_N , εc_T and f on stability

Here, we recall that the equation of motion (1) was obtained using the assumption that the coefficients associated with friction in the normal and tangential directions, c_N and c_T

respectively, are equal; hence, they were replaced by the friction coefficient c_f , and all the matrices were defined using εc_f . Thus, in order to study the effects on stability of the normal and tangential viscous parameters, εc_N and εc_T respectively, the mass, damping and stiffness matrices need to be defined again (refer to Appendix E).

The calculations were carried out with $\varepsilon=20$ in order to consider a slender cylinder. The dimensionless critical flow velocities for first mode divergence (buckling) and second mode flutter through a Hopf bifurcation were investigated for two different ratios c_N/c_T , and for different values of the slenderness parameter f.

Figure 5(a,b) shows the evolution of the dimensionless critical flow velocity for divergence, for $c_N/c_T=0.5$ and $c_N/c_T=2$. In both cases we note that the critical flow velocity increases with the parameter εc_N , leading to a more stable system. Furthermore, if εc_N is fixed to a certain value, say $\varepsilon c_N=8$ for $c_N/c_T=0.5$ and $\varepsilon c_N=0.5$ for $c_N/c_T=2$, decreasing f will stabilize the system. In some other ranges, however, e.g. for $0<\varepsilon c_N<5$ for $c_N/c_T=0.5$ (Figure 5(a)), the effect can be rather weak. Generally, however, a less well streamlined free end has a stabilising effect in both cases.

In the case of $c_N/c_T=0.5$, we notice that each f-curve converges to a limit value of εc_N . Thus, for instance, if $\varepsilon c_N \ge 13$ divergence will only occur for $f \ge 0.9$. Moreover, first mode restabilization is predicted only for $\varepsilon c_N < 3.5$, approximately. In contrast, for $c_N/c_T=2$ each f-curve $(f \ne 1)$ is composed of a lower branch and an upper branch that coalesce, corresponding respectively to the loss and the regaining of stability. The curve for f=1, compared to the others, seems to be a degenerate case, since the upper and lower branches

diverge from each other. Finally, and most importantly, divergence for $c_{N} / c_{T} = 2$ occurs at higher flow velocities.

Figure 6(a,b) shows the critical flow velocities for second mode flutter through a Hopf bifurcation, for $c_N / c_T = 0.5$ and $c_N / c_T = 2$. Here also, increasing the parameter εc_N stabilizes the system. However, we observe two definitely different types of evolution.

For $c_N/c_T=0.5$ we notice in Figure 6(a) that the longest stability curves correspond to the lowest f; e.g., for $\varepsilon c_N>1$ flutter only occurs for f<0.8. Actually, increasing the slenderness parameter f reduces the interval of εc_N over which flutter is possible. Hence, a well streamlined free end and a high viscous parameter, e.g. f>0.8 and $\varepsilon c_N>1$, will also stabilize the system - as well as a very small f.

We should also mention that the stability curves cross one another for small flow velocities. Actually, for f < 0.8 we notice that the stability curves behave in a peculiar manner, e.g. that for f = 0.9 is lower than the branch for f = 0.8 and still lower than the branch for f = 0.97. No particular reason for this behaviour has been found.

In the case of $c_N/c_T=2$ (Figure 6(b)), a similar phenomenon is observed, but it is less prominent. Here, we observe that the longest curves correspond to the highest f, e.g. for $\varepsilon c_N > 3$ flutter only occurs for $f \ge 0.8$. Moreover, the upper branch in each f-curve shows that stability can be regained. Ultimately, we may notice that there are some qualitative similarities between Figures 5(b) and 6(b).

The conclusion is that if $c_N \neq c_T$, quite different results are obtained for $c_N > c_T$ and $c_N < c_T$.

4.2.3 Effects of β and f on stability

The mass ratio parameter, β , has no effect on the critical flow velocity for divergence. Hence, only its effect on critical flow velocities for flutter is investigated. These results were obtained for $\varepsilon c_N = \varepsilon c_T = 1$.

Figure 7 shows that increasing β stabilizes the system but not drastically; it is recalled that β cannot be larger than 1. We also observe that a blunt end, i.e., a less well streamlined free end, has a stabilising effect.

Following a curve, for instance the curve corresponding to f = 0.6, we notice that loss, regaining and even new loss of stability are possible. This does not occur for $f \ge 0.7$, since the limit point where instability and restabilization become coincident occurs for $\beta > 1$, which is not physical. Moreover, with the aid of the results obtained when we investigated the effects of f by itself (see Figure 3), we can add here that no regaining of stability is predicted for f > 0.83 approximately. This is why, in the curve corresponding to f = 0.9, we just observe one branch.

Furthermore, it should be mentioned that the curve corresponding to f=0.9 crosses the other curves at $\beta \le 0.5$; i.e. a larger f, e.g. f=0.9, seems to stabilize the system compared to a smaller one e.g. f=0.8. This peculiar behaviour seems to occur only for f>0.8.

The stability of the cantilevered cylinder has been widely investigated. Apart from some peculiar results, especially concerning flutter instabilities, we can conclude that a blunt free end, a large viscosity parameter εc_N as well as a high mass ratio β , all have stabilising effects.

Now, it is of interest to study the nonlinear dynamics and observe the behaviour of this system after the loss of stability. Emphasis is put mainly on peculiar types of dynamical behaviour.

5. NONLINEAR DYNAMICS

5.1 NUMERICAL METHODS

Here, two methods are used in order to solve the equations of motion and obtain accurate numerical solutions: a finite difference method (FDM) and a collocation method (the software package AUTO [5]), the latter being very efficient in continuation and bifurcation problems in ordinary differential equations.

A fourth-order finite difference method (FDM4), known also as Houbolt's finite difference method [6], is employed. The derivatives at time $\tau + \Delta \tau$ are replaced by backward difference formulae using, in this case, values at three previous time steps $\Delta \tau$, respectively. The fourth order scheme is commonly defined by

$$\ddot{q}_{j}(\tau + \Delta \tau) = \sum_{p=0}^{p=n} \alpha_{p+1} q_{j}(\tau + (1-p)\Delta \tau) / (\Delta \tau)^{2},$$

$$\dot{q}_{j}(\tau + \Delta \tau) = \sum_{p=0}^{p=n} \beta_{p+1} q_{j}(\tau + (1-p)\Delta \tau) / (\Delta \tau),$$

(15)

with n = 3, and where α_p and β_p are defined in Table 1.

Substitution of (15) into (10) leads to a set of nonlinear algebraic equations of the type

$$F_{i}\left[q_{i}(\tau + \Delta\tau), q_{i}(\tau), q_{i}(\tau - \Delta\tau), q_{i}(\tau - 2\Delta\tau), \ldots\right] = 0, \quad 1 \le i, j \le N,$$

in which $q_j(\tau + \Delta \tau)$ are the unknowns. In order to solve equation (16) the Newton-Raphson method is employed, taking as initial guess for $q_j(\tau + \Delta \tau)$ the value of its predecessor, $q_j(\tau)$. Note that the Newton-Raphson method requires the computation of the Jacobian of F, $\left[\partial F_i / \partial q_j(\tau + \Delta \tau)\right]$. This can be obtained easily from (16); (refer to Semler et~al. [7]).

5.2 NONLINEAR DYNAMICAL BEHAVIOUR OF CANTILEVERED CYLINDERS

We shall use the numerical methods afore-mentioned in order to study the nonlinear dynamics by means of bifurcation, phase portrait, power spectrum and displacement-versus-time diagrams. These diagrams will enable us to have a kaleidoscopic view of the behaviour of the system under consideration.

We shall first here consider a set of parameters modeling a system close to one studied in an experiment conducted by Païdoussis *et al.* [8], then discuss briefly other sets of parameters leading to results that deserve to be mentioned.

5.2.1 Comparison with an experience

The parameters are set at f=0.7, $\beta=0.47$, $\varepsilon c_f=0.5$, $c_d=0$, $\gamma_C=14.35$, $\gamma_F=12.51$, $\chi_e=0.00667$, $\overline{\chi}_e=0.00785$, $\zeta_b=(1-f)=0.3$, $\zeta_b=1$, and $\zeta_b=0$, which are close to an experimentally studied system [8]. Two different Galerkin approximations are here used showing that increasing the flow velocity requires further modes in order to describe the behaviour of the system.

4-mode approximation

A typical bifurcation diagram of the system is shown in Figure 8, computed with AUTO using a 4-mode Galerkin approximation. The bifurcations of the zero solution correspond to the critical velocities for the onset of instabilities obtained with the linear theory, and are as follows: the critical flow velocity for first-mode divergence, $U_{cd} = 2.29$ (BP1); for first-mode restabilization, $U_{cf1} = 5.62$ (HB1) and $U_{cf2} = 9.17$ (HB2), respectively; for second-mode restabilization, $U_{cf1} = 9.14$ (HB3).

The branch corresponding to the position of rest of the system is labelled in Figure 8 as "initial equilibrium". This branch is stable for $\mathcal{U} \leq \mathcal{U}_{cd}$. Small axial flow velocities generate flow-induced damping; hence, after some transients, the system converges to the initial stable state (see Figure 9(a) for $\mathcal{U}=2.0$). Then, at $\mathcal{U}=\mathcal{U}_{cd}$ (BP1) the initial equilibrium state becomes unstable and the system diverges in its first mode. From thereon develops a stable static branch, labelled "1st mode", which actually represents a set of successive fixed points (each dependent on the actual \mathcal{U}). The mirror image of this branch, also drawn in Figure 8, represents divergence on the other side of equilibrium. This is illustrated with Figure 9(b) for $\mathcal{U}=4$, where the system converges to a stable fixed point. We observe that the displacement of the tip does not exceed 40% of the total length of the cantilever, which is reasonable and in agreement with the experiments conducted by Païdoussis *et al.* [8]. Moreover, we notice that the first-mode locus is a closed curve, showing that the amplitude increases first and then decreases to zero.

At U = 5.33 (BP2), the first mode regains stability as predicted by the linear theory in Section 4.1. Furthermore, Figure 8 shows that, actually, the system itself recovers stability, i.e., for velocities slightly higher than 5.33 any perturbation will die out and lead the system to its

position of rest. See, for instance, Figure 10 for $\mathcal{U}=5.55$ where the displacement converges to zero, and notice the trajectory, which is representative of damped oscillatory motion. Actually, this behaviour shows influence of the second-mode flutter in the waviness of the large oscillations, which follows at higher \mathcal{U} .

At U=5.62 (HB1), second-mode flutter occurs through a Hopf bifurcation. The initial equilibrium state loses again stability and a new branch, labelled "2nd mode", emerges from the Hopf bifurcation point: these are "dynamic" solutions, representing periodic motions of the system. Figure 11(a-f) show periodic displacement of the tip with respect to time at U=6 and at a higher flow velocities U=6.5 and U=7.5, supplemented by phase-plane plots at same velocities, which show symmetric limit cycle oscillations. We notice that the amplitude of the oscillations is of the same order of magnitude as the amplitude for divergence.

Eventually, the second-mode locus loses stability through a torus at $\mathcal{U}=8.51$ (T), while the branch emerging from the third-mode Hopf bifurcation at $\mathcal{U}=9.17$ (HB2), labelled "3rd mode", is unstable all along (except in a very narrow range around $\mathcal{U}=8.5$). Hence, from thereon, according to this 4-mode approximation, there is no possible new stable solution, which is not physically acceptable.

Furthermore, an experiment conducted by Païdoussis *et al.* [8] corresponding to this set of parameters showed that second-mode flutter is followed by third-mode flutter at higher flow velocities. Therefore, in order to capture this dynamical behaviour, the Galerkin discretisation is now undertaken with a 5-mode approximation.

5-mode approximation

Figure 12 shows the bifurcation diagram of the system, computed with AUTO using a 5-mode Galerkin approximation. Again, the bifurcations of the zero solution correspond to the critical

velocities for the onset of instabilities obtained with the linear theory (the same as aforementioned, but with slightly differences), and are as follows: the critical flow velocity for first-mode divergence, $\mathcal{U}_{cd} = 2.29$ (BP1); for first-mode restabilization, $\mathcal{U} = 5.3$ (BP2); for secondand third-mode flutter via a Hopf bifurcation, $\mathcal{U}_{cf1} = 5.6$ (HB1) and $\mathcal{U}_{cf2} = 9.06$ (HB2) respectively; for second-mode restabilization, $\mathcal{U} = 9.14$ (HB3).

Using this 5-mode approximation, the second-mode locus still loses stability through a torus at $\mathcal{U}=8.53$ (T) but, just before that, the third-mode locus, which arises from a *subcritical* Hopf bifurcation at $\mathcal{U}=9.06$, becomes stable at $\mathcal{U}=8.46$ leading to third-mode flutter. Hence, adding one mode in the Ritz-Galerkin solution enables one to obtain stable solutions for higher flow velocities, namely third-mode flutter in this case.

We notice that the amplitude of the oscillations in third mode is lower than in second mode, this also being in agreement with the experiments conducted by Païdoussis *et al.* [8]. Moreover, for $8.46 \le \mathcal{U} \le 8.53$ there coexist competing attractors corresponding to second- and third-mode flutter (here it is noted that the mode nomenclature simply follows continuity of locus from $\mathcal{U}=0$ to higher \mathcal{U}). This indicates that in the vicinity of $\mathcal{U}=8.5$ interesting nonlinear dynamical behaviour may be expected.

Figure 13(a) shows a phase-plane diagram for $\mathcal{U}=8.5$ with quasiperiodic-looking trajectories. However, the behaviour of the system for this flow velocity seems slightly chaotic. We see that the power spectrum in Figure 13(b) shows at least four irrationally-related frequencies; actually, as pointed out by Ruelle & Takens [9], a chaotic attractor may be observed after the birth of a three-period quasiperiodic attractor. Moreover, the Poincaré map in Figure 13(c), obtained with trigger that the generalized displacement q_2 be zero, is representative of a weakly chaotic regime by its definite structure and finite-banded width, in contrast to a random

process. Therefore, we may conclude that, in the vicinity of the transition from second- to third mode-flutter, quasiperiodic oscillations leading to chaotic motions may occur. This is to be contrasted to the clearly quasiperiodic phase-plot of Figure 14 at U = 8.529.

At $\mathcal{U} = 9.75$, the third mode locus becomes unstable through a transcritical bifurcation, and the q_1 versus \mathcal{U} curve displays a discontinuity leading to another stable solution.

An unstable divergence solution begins at $\mathcal{U}=9.66$ (BP3), sharply increases in amplitude, then decreases, and eventually ceases at $\mathcal{U}=12.86$ (BP4). From this unstable solution, a stable oscillatory solution branch is generated via a Hopf bifurcation at $\mathcal{U}=9.98$, and exists briefly, before itself becoming unstable through a torus at $\mathcal{U}\sim9.9$.

After $\mathcal{U} \sim 10.8$, there appears to exist no stable solution. This does not signal the onset of generalized chaos. It more likely means that the 5-mode Galerkin approximation is insufficient to properly model fourth-mode behaviour; providing enough modes are used, some new stable solutions could then be found. Again, it is noted that the mode nomenclature simply follows continuity of locus from $\mathcal{U} = 0$ to higher \mathcal{U} ; but, for $\mathcal{U} \sim \mathcal{O}(10)$, the third mode for instance contains considerable amounts of fourth and fifth beam-mode content, the latter of which is probably inadequately predicted [4].

5.2.2 Further discussions

The nonlinear dynamics are also investigated for some other sets of parameters, namely modeling systems close to the previous one (studied in Section 5.2.1), but with a more or less well streamlined free end and higher or lower viscous parameters. A 5-mode Galerkin approximation is used in all cases.

Figure 15 shows a bifurcation diagram of the system for f=0.6, $\varepsilon c_f=0.25$, $c_b=(1-f)=0.4$ the other parameters keeping the same values as in Section 5.2.1 (the nomenclature of the branches and points follows that of Figure 8). In this case, we notice that the second-mode locus is stable all the way from $\mathcal{U}_{cf1}=5.77$ (HB1) to $\mathcal{U}=9.02$ (HB2). Furthermore, the third-mode locus, which arises from a subcritical Hopf bifurcation point at $\mathcal{U}_{cf2}=9.14$ (HB3), is preceded by the restabilization of the initial equilibrium state. Here, the transition from second- to third-mode flutter is not as significant as in the previous case. However, competing attractors corresponding to second- and third-mode flutter and even to the initial equilibrium state still coexist over a narrow-flow range.

Increasing the slenderness parameter f to 0.7 (changing c_b to 0.3) with the other parameters remaining unchanged provides a bifurcation diagram – see Figure 16 - similar to the one in Figure 12, including the development of third-mode flutter and transition from second- to third-mode flutter. However, in this case the second mode locus is not continuous all along, but undergoes a "burst" around its maximum, dividing the second-mode locus into two disjoint branches. The physical nature of this phenomenon is not clear.

Similar odd results are also obtained when setting f equal to 0.8 (and c_b to 0.2) and increasing εc_f to 0.5. Here, the second-mode locus which arises from a *subcritical* Hopf bifurcation is unstable and strongly perturbed by the "burst". Consequently, there is no stable solution immediately after first-mode restabilization and, due to the "burst", second-mode flutter only develops in the second branch. Finally, third-mode flutter only materializes over a narrow-flow range.

These last two results contrast with those described in Section 5.2.1 which are in agreement with some experiments conducted recently. Unfortunately, we are not presently able to provide any explanation to this peculiar behaviour.

6. CONCLUSION

The equation of motion derived enabled us to study for the first time some aspects of the nonlinear dynamics of a cantilevered cylinder in axial flow. The stability of the system as well as the influence of some parameters were investigated; this was followed by a modest exploration of the nonlinear dynamics of the system.

Some good qualitative agreement was found with the experiments, especially concerning the amplitude of the oscillations, and whether restabilization ranges exist between the various zones of linear unstable behaviour. Moreover, with the aid of a 5-mode Galerkin approximation, interesting nonlinear behaviour was observed in the vicinity of the transition from second- to third-mode flutter, showing quasiperiodic and weakly chaotic motion. The possible existence of chaos in that vicinity was also remarked in the experiments (and is evident in available videos), but was never proved.

Finally, it was found that higher flow velocities require more accurate Galerkin approximations in order to obtain stable solutions. In particular, it is expected that the non-physical finding that no stable solution exists beyond a certain value of flow velocity is due to an insufficient number of terms in the Galerkin expansion.

This is mainly a first step in the study of the nonlinear dynamics of a cylinder immersed in flowing fluid. A great deal of calculations remain to be done, to exploit the model developed in

this report. Another studies for different sets of parameters for inextensible cantilevers are likely to be investigated and compared to results obtained with the extensible model and also to some new experiments. It is hoped that they will be done in the near future.

REFERENCES

- [1] J.L. Lopes, M.P. Païdoussis & C. Semler 1999 Nonlinear equations of a cylinder in steady axial flow. MERL Report No. 99-1, Department of Mechanical Engineering, McGill University.
- [2] M.P. Païdoussis 1966 *Journal of Fluid Mechanics* 26, 717-736. Dynamics of flexible slender cylinders in axial flow. Part 1: Theory.
- [3] M.P. Païdoussis 1973 *Journal of Sound and Vibration* 29, 365-385. Dynamics of cylindrical structures subjected to axial flow.
- [4] M.P. Païdoussis 1998 Fluid-Structure Interactions: Slender Structures and Axial Flow, Volume 1. London: Academic Press.
- [5] E.J. Doedel & J.P. Kernéves 1986 Applied Mathematics Report, California Institute of Technology, Pasadena, California, U.S.A. AUTO: software for continuation and bifurcation problems in ordinary differential equations (can be obtained from Doedel@cs.concordia.ca).
- [6] J.C. Houbolt 1950 *Journal of Aeronautical Sciences* 17, 540-550. A recurrence matrix solution for the dynamic response of elastic aircraft.
- [7] C. Semler, W.C. Gentleman & M.P. Païdoussis 1996 *Journal of Sound of Vibration* 195, 553-574. Numerical solutions of second order implicit non-linear ordinary equations.

- [8] M.P. Païdoussis, D. Adamovic & E. Grinevich 1999. An experimental study of the dynamics of cantilevered cylinders in axial flow (in preparation).
- [9] D. Ruelle & F. Takens 1971 *Communication in Mathematics and Physics* 20, 167-192. On the nature of turbulence.
- [10] R.E.D. Bishop & D.C. Johnson 1979 The Mechanics of Vibration. New York: Cambridge University Press.

TABLES

Table 1: The coefficients of the fourth order finite difference method

Acceleration coefficients	Velocity coefficients
$\alpha_1 = 2$	$\beta_1 = 11 / 6$
$\alpha_2 = -5$	$\beta_2 = -18 / 6$
$\alpha_3 = 4$	$\beta_3 = 9/6$
$\alpha_4 = -1$	$\beta_4 = -2/6$

FIGURES

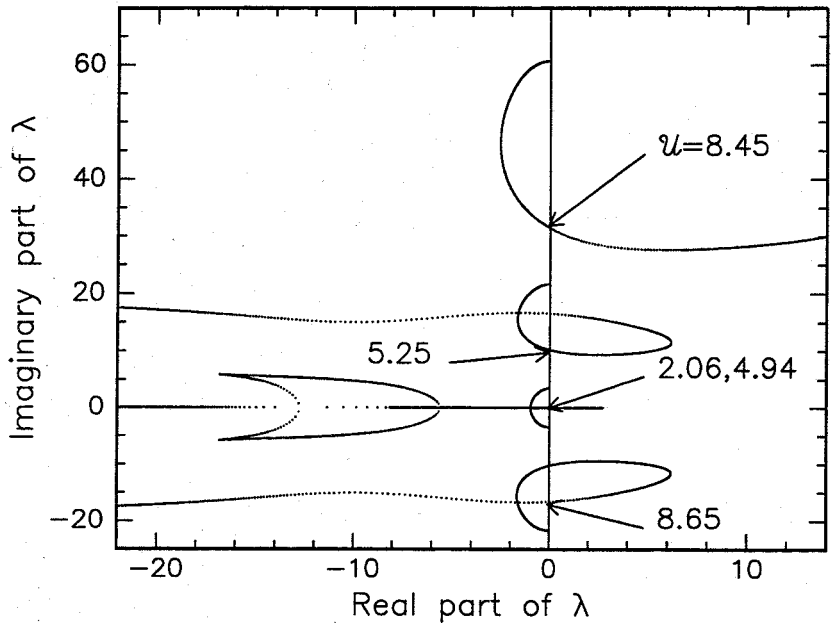


Figure 1: Typical Argand diagram showing the dimensionless eigenvalues λ of the lowest three modes with flow velocity $\mathscr U$ as parameter for an inextensible cantilevered cylinder. The other parameters are set at f=0.8, $\beta=0.5$, $\chi=1$, h=0, $\varepsilon c_f=1$, $\chi_e=0.01$, $\overline{\chi}_e=0.01$, $c_b=0$ and $\gamma_C=\gamma_F=0$.

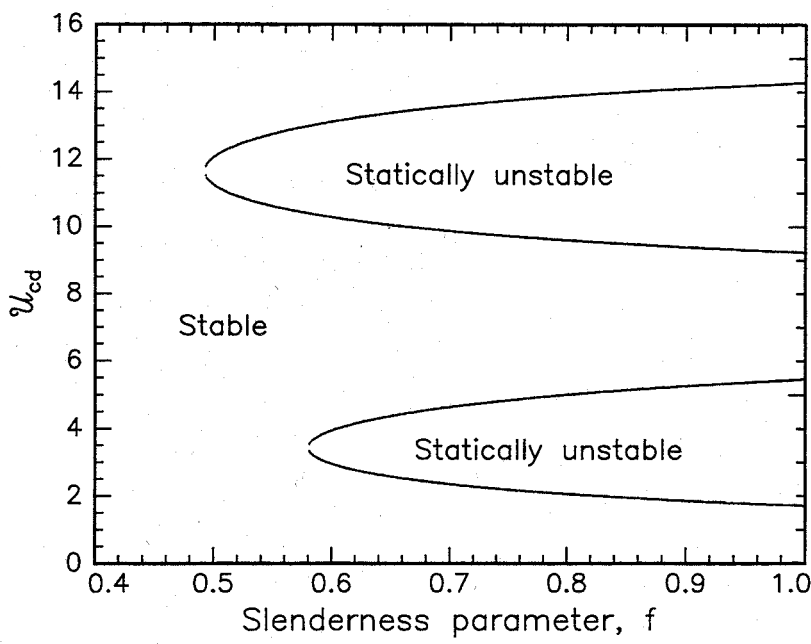


Figure 2: The dimensionless critical flow velocity for buckling of a cantilevered cylinder, showing the effects of f for $\chi=1$, h=0, $\varepsilon c_f=1$, $\chi_e=0.00667$, $\overline{\chi}_e=0.00785$, $c_b=0$ and $\gamma_C=\gamma_E=0$.

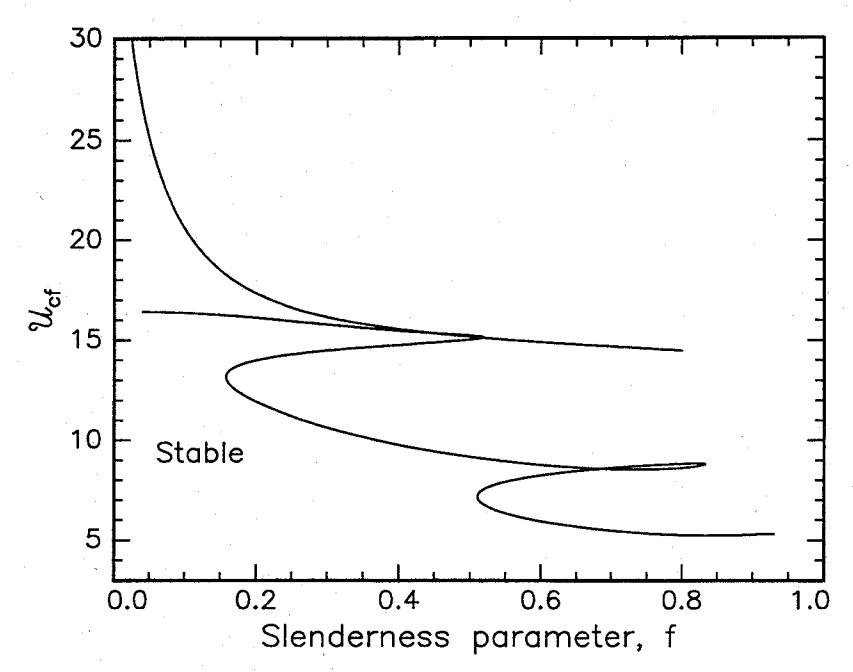


Figure 3: The dimensionless critical flow velocity for flutter through a Hopf bifurcation of a cantilevered cylinder, showing the effects of f for $\beta=0.5$, $\chi=1$, h=0, $\varepsilon c_f=1$, $\chi_e=0.00667$, $\overline{\chi}_e=0.00785$, $c_b=0$ and $\gamma_c=\gamma_F=0$.

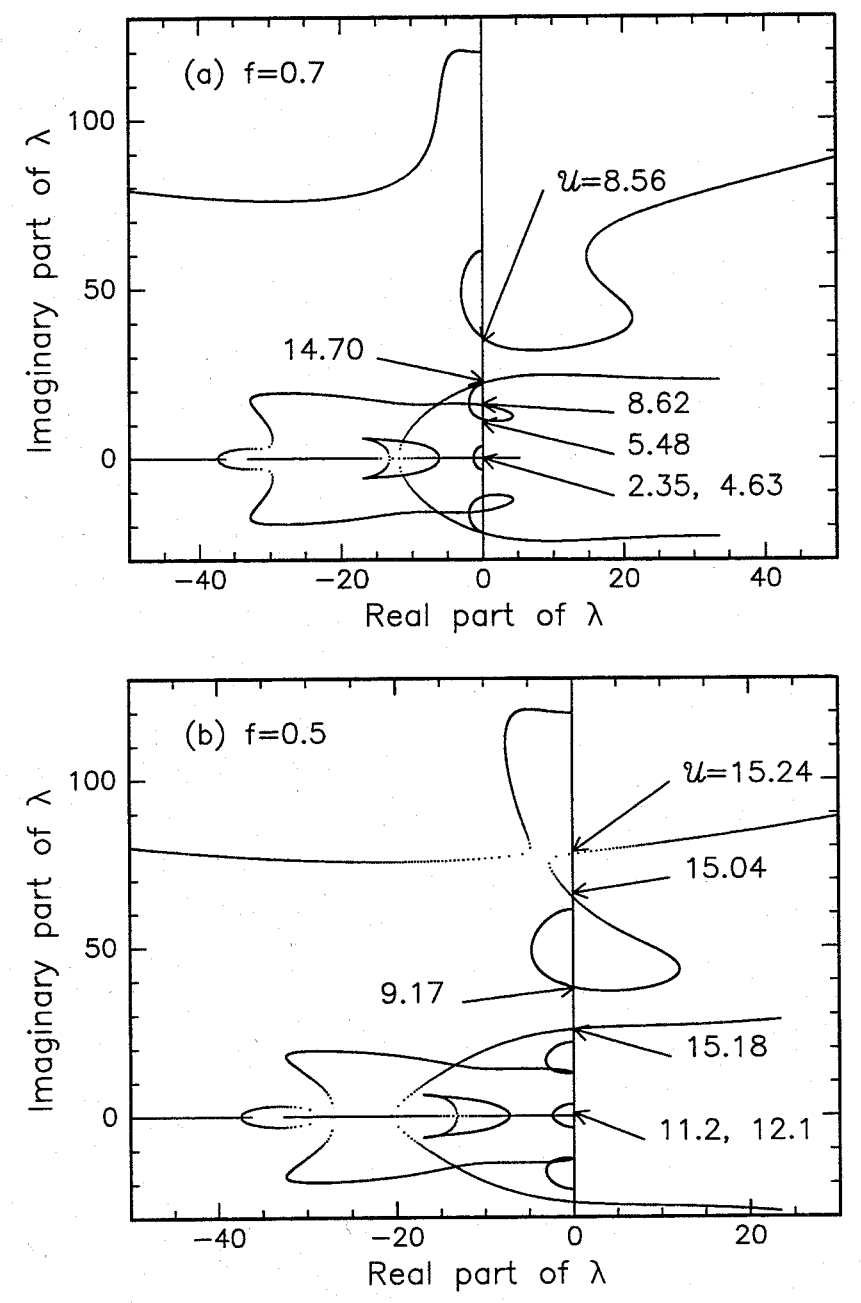


Figure 4: Argand diagrams showing the dimensionless complex eigenvalues λ of the four lowest modes of a cantilevered cylinder for (a) f=0.7, and (b) f=0.5, the other parameters being set at $\beta=0.5$, $\chi=1$, h=0, $\varepsilon c_f=1$, $\chi_e=0.00667$, $\overline{\chi}_e=0.00785$, $c_b=0$ and $\gamma_C=\gamma_F=0$.

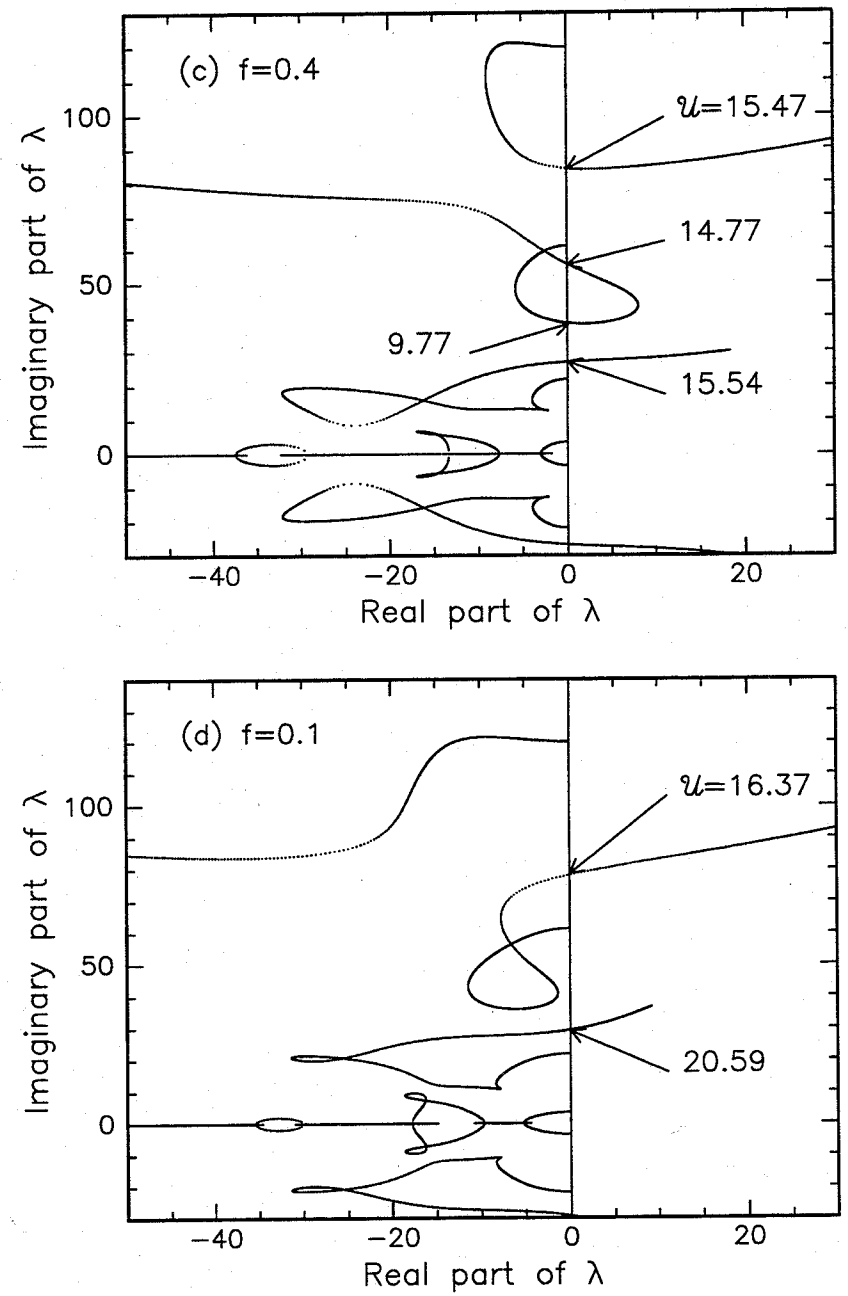


Figure 4: (Continued) Argand diagrams showing the dimensionless complex eigenvalues λ of the four lowest modes of a cantilevered cylinder for (c) f=0.4, and (d) f=0.1, the other parameters being set at $\beta=0.5$, $\chi=1$, h=0, $\varepsilon c_f=1$, $\chi_e=0.00667$, $\overline{\chi}_e=0.00785$, $c_b=0$ and $\gamma_c=\gamma_F=0$.

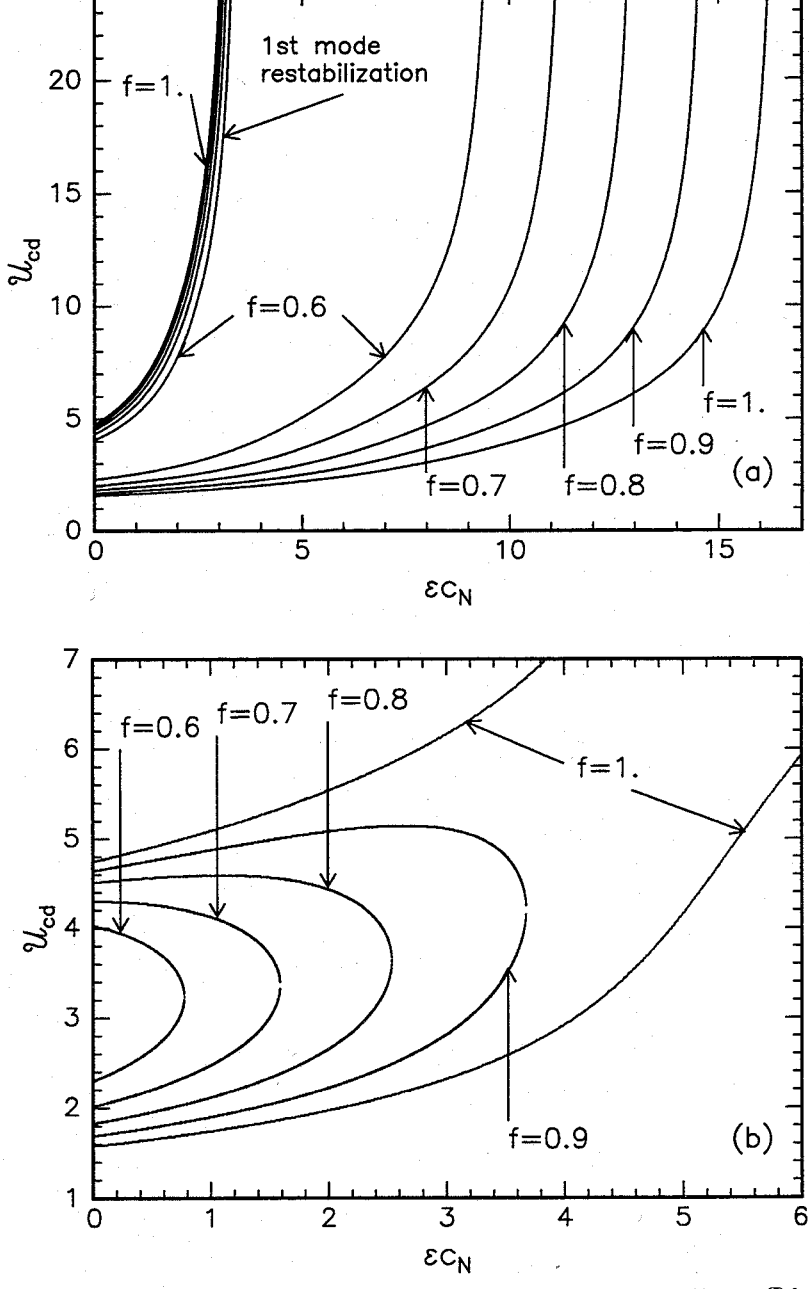


Figure 5: The dimensionless critical flow velocity for divergence (buckling) \mathcal{U}_{cd} of a cantilevered cylinder for (a) c_N / c_T = 0.5, and (b) c_N / c_T = 2, showing the effects of f and εc_N on stability. The other parameters are set at $\chi=1$, h=0, $\chi_e=0.00667$, $\overline{\chi}_e=0.00785$, $c_b=0$ and $\gamma_C=\gamma_F=0$.

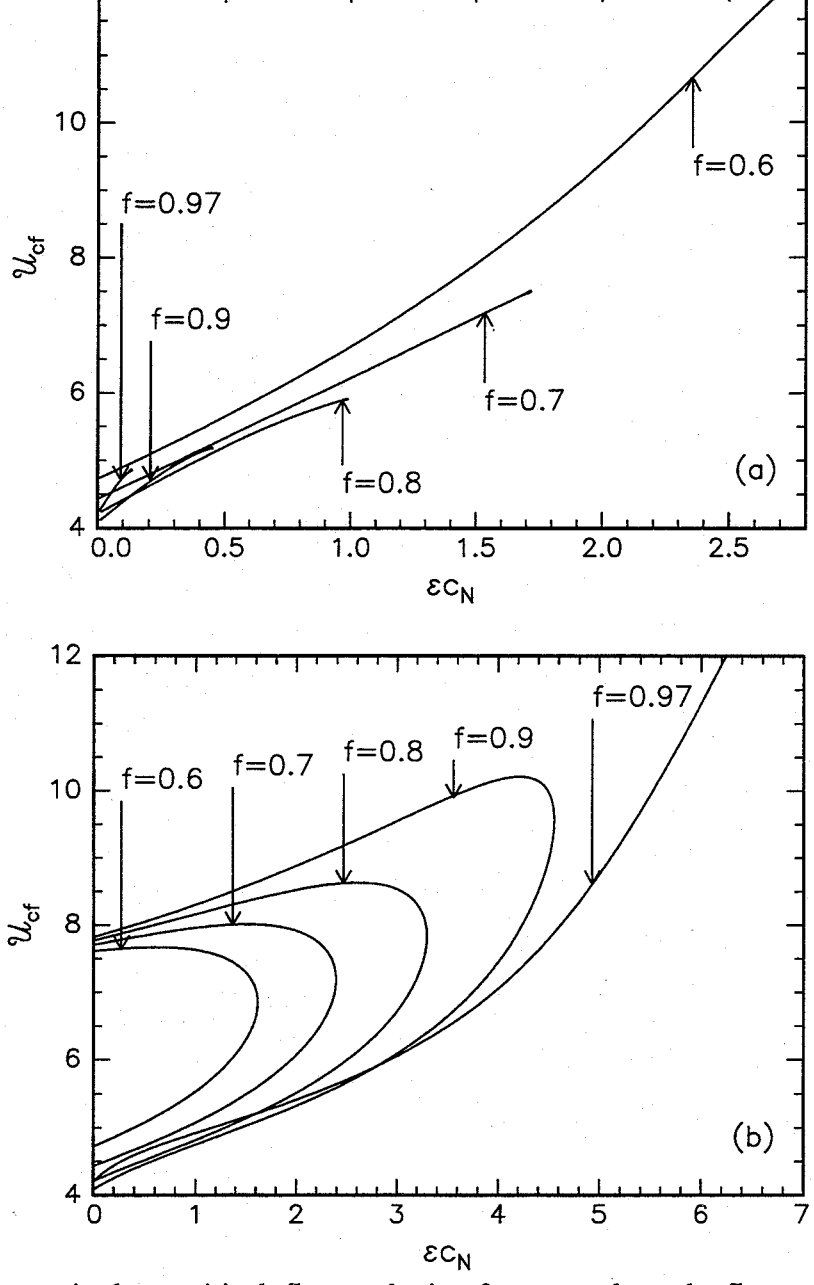
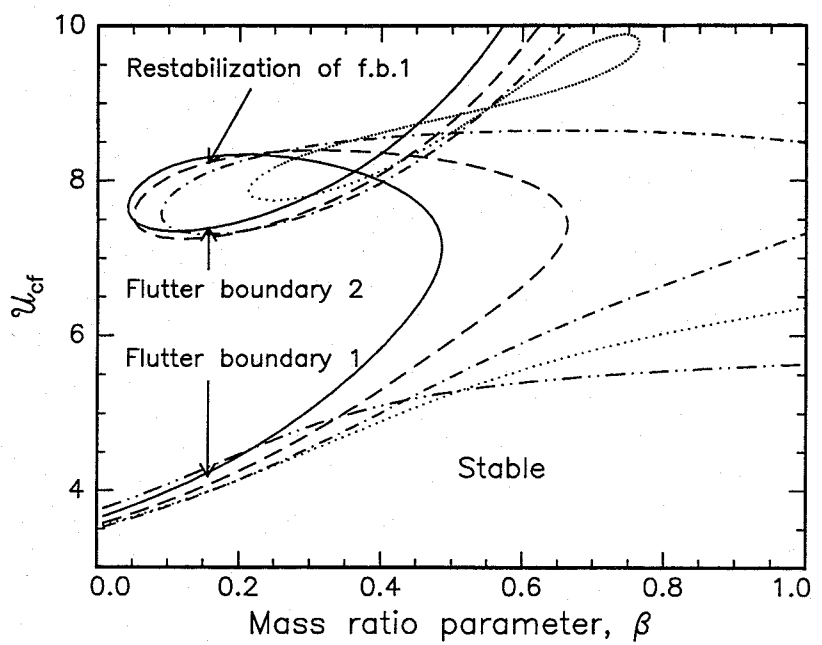


Figure 6: The dimensionless critical flow velocity for second mode flutter through a Hopf bifurcation \mathscr{U}_{cf} of a cantilevered cylinder for (a) c_N / c_T = 0.5, and (b) c_N / c_T = 2, showing the effects of f and εc_N on stability. The other parameters are set at β = 0.5, χ = 1, h = 0, χ_e = 0.00667, $\overline{\chi}_e$ = 0.00785, c_b = 0 and γ_C = γ_F = 0.



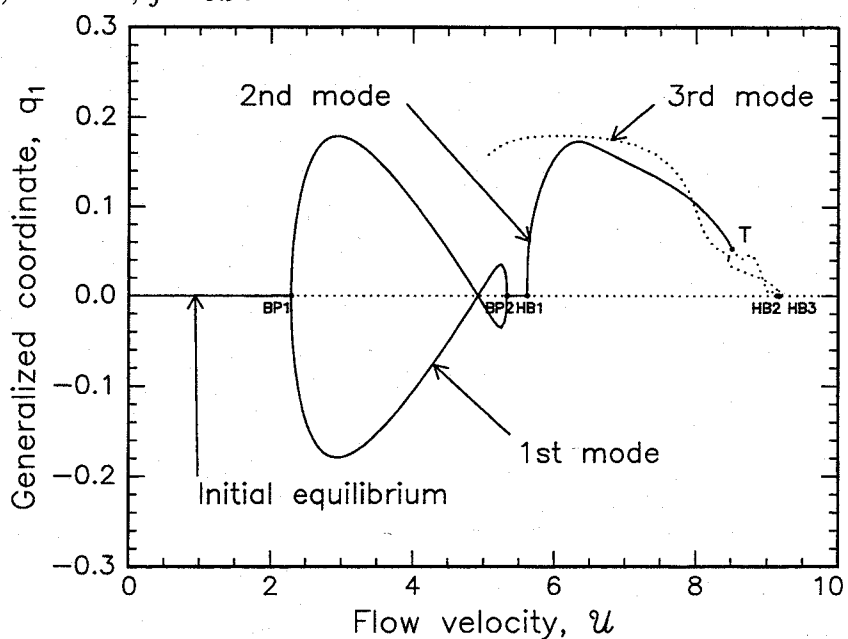


Figure 8: Bifurcation diagram for f=0.7, $\beta=0.47$, $\varepsilon c_f=0.5$, $\chi=1$, h=0, $\chi_e=0.00667$, $\overline{\chi}_e=0.00785$, $c_b=0.3$, $c_d=0$, $\gamma_c=14.4$, and $\gamma_F=12.5$, computed with 4 modes, showing the first generalized co-ordinate versus \mathscr{U} : ———, stable solution; ……, unstable solution.

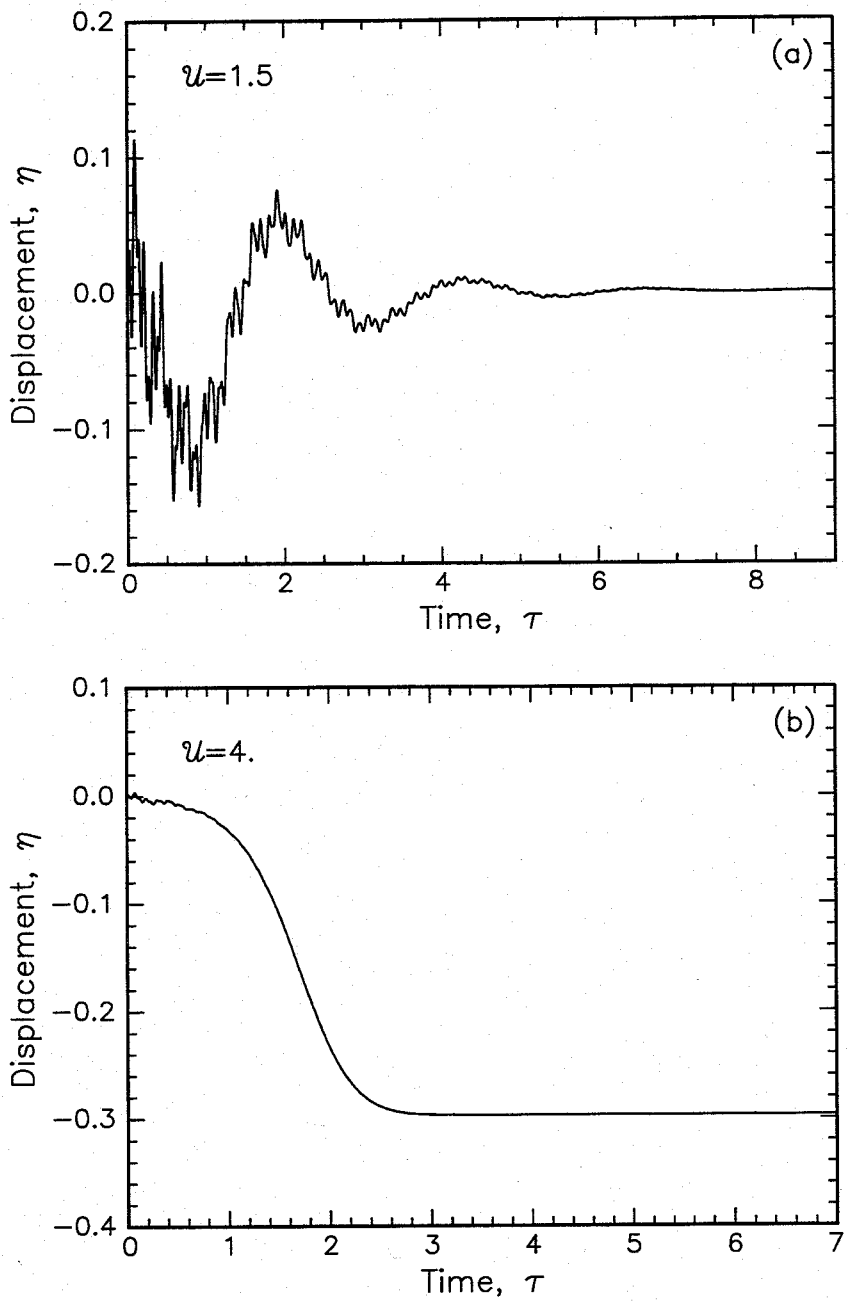


Figure 9: Displacement-versus-time diagram for (a) $\mathcal{U}=1.5$ and (b) $\mathcal{U}=4$; the parameters are set at f=0.7, $\beta=0.47$, $\varepsilon c_f=0.5$, $\chi=1$, h=0, $\chi_e=0.00667$, $\overline{\chi}_e=0.00785$, $c_b=0.3$, $c_d=0$, $\gamma_C=14.4$, and $\gamma_F=12.5$.

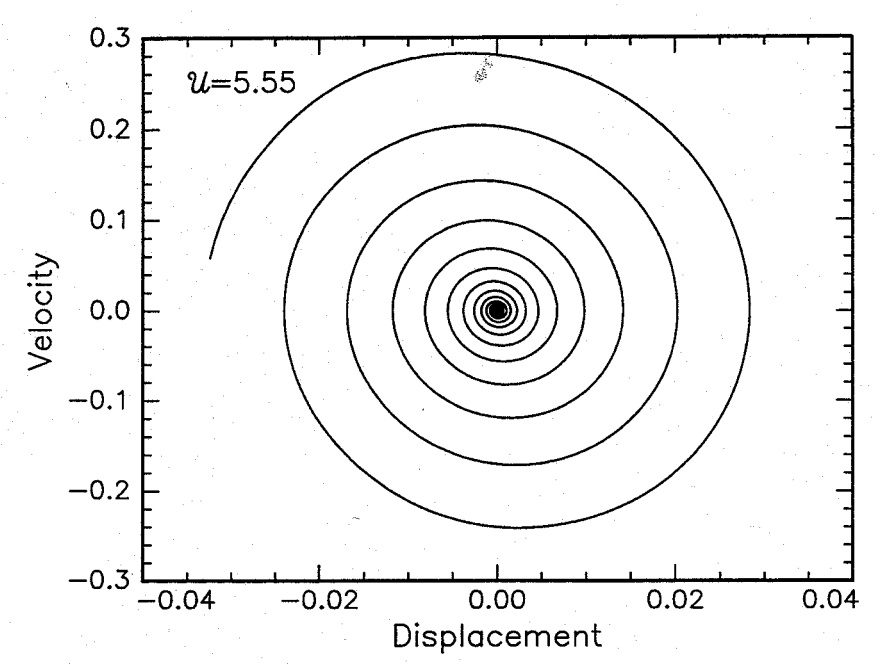


Figure 10: Phase portrait diagram for $\mathcal{U}=5.55$; the parameters are set at f=0.7, $\beta=0.47$, $\varepsilon c_f=0.5$, $\chi=1$, h=0, $\chi_e=0.00667$, $\overline{\chi}_e=0.00785$, $c_b=0.3$, $c_d=0$, $\gamma_C=14.4$, and $\gamma_F=12.5$.

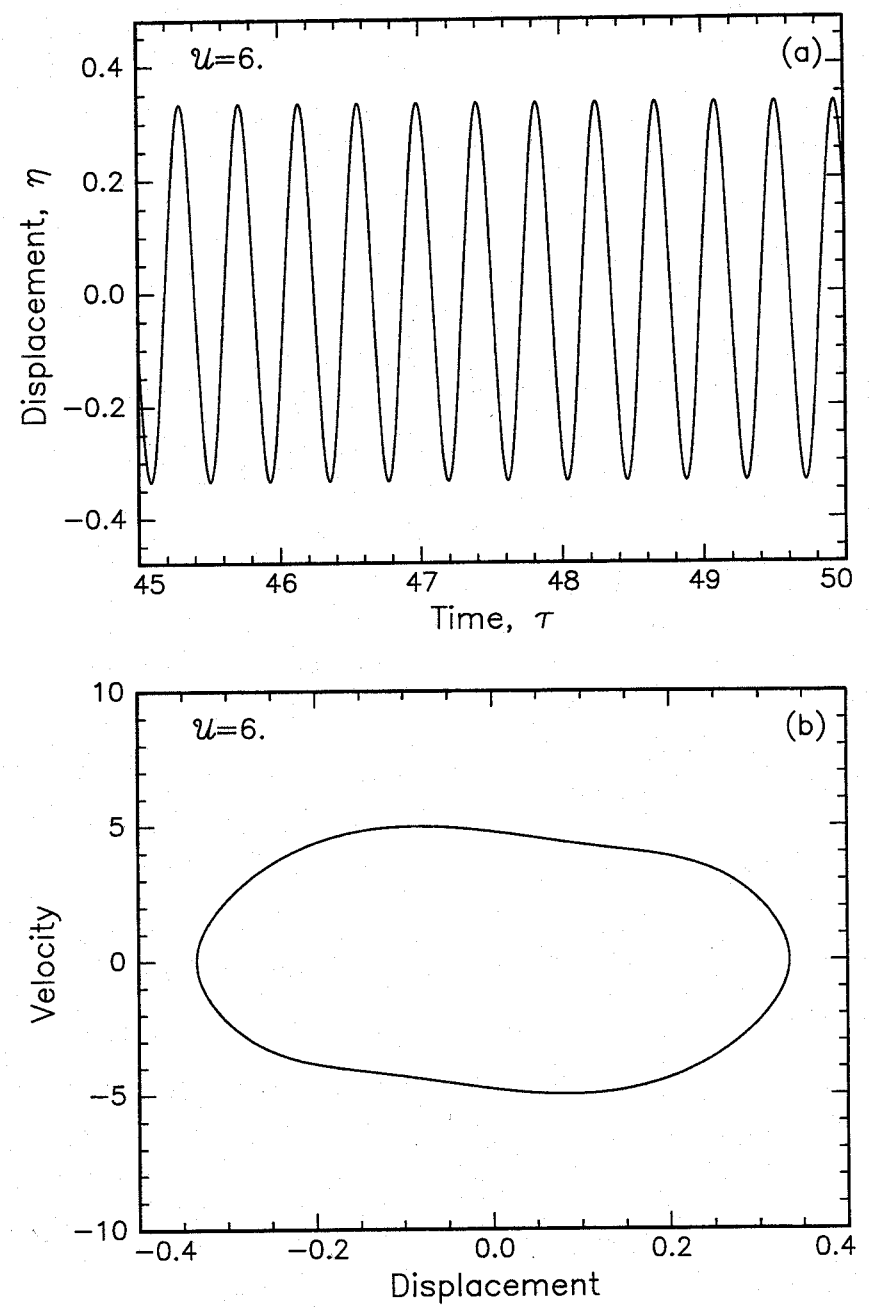


Figure 11: (a) Displacement-versus-time diagram and (b) phase portrait diagram for $\mathcal{U}=6$; the parameters are set at f=0.7, $\beta=0.47$, $\varepsilon c_f=0.5$, $\chi=1$, h=0, $\chi_e=0.00667$, $\overline{\chi}_e=0.00785$, $c_b=0.3$, $c_d=0$, $\gamma_C=14.4$, and $\gamma_F=12.5$.

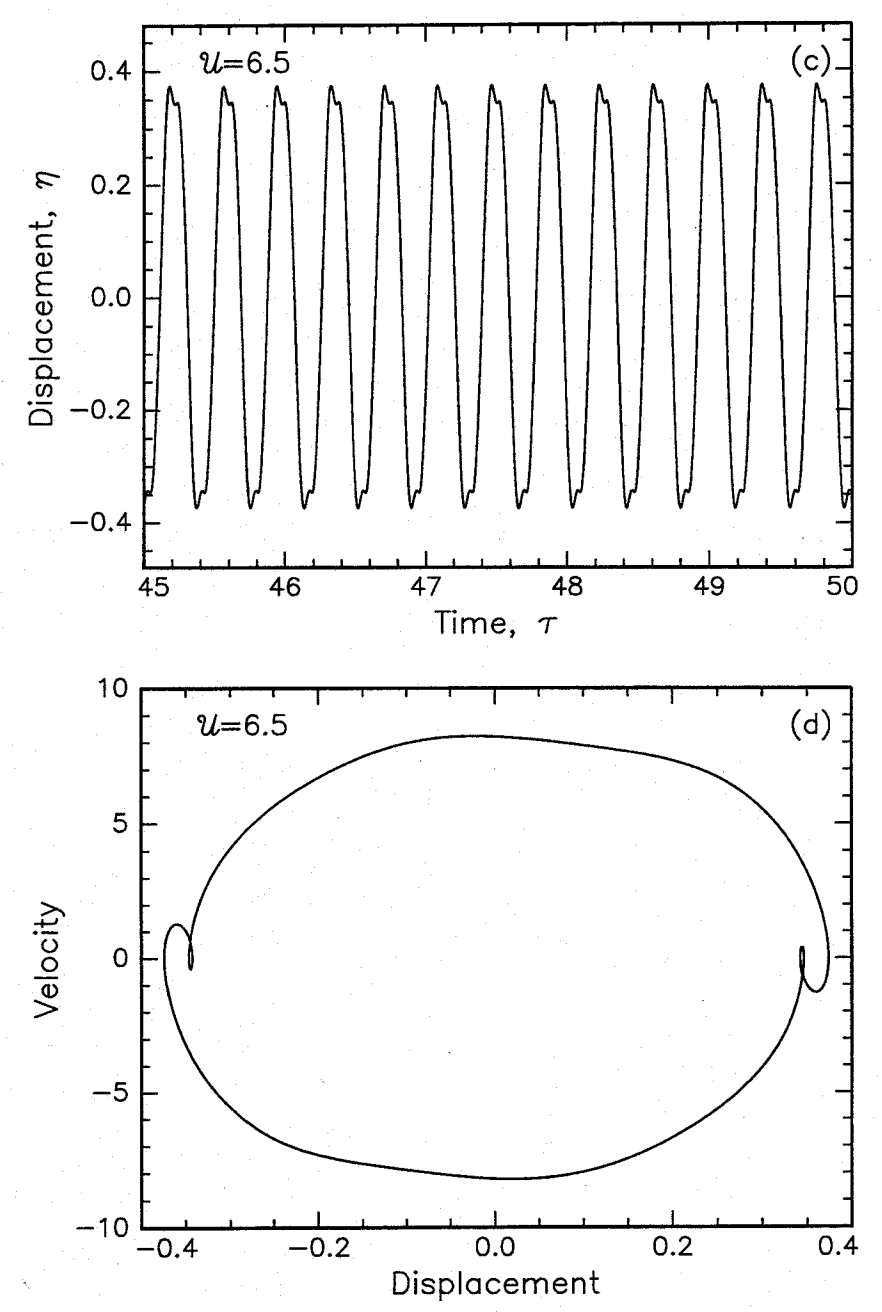


Figure 11: (c) Displacement-versus-time diagram and (d) phase portrait diagram for $\mathscr{U}=6.5$; the parameters are set at f=0.7, $\beta=0.47$, $\varepsilon c_f=0.5$, $\chi=1$, h=0, $\chi_e=0.00667$, $\overline{\chi}_e=0.00785$, $c_b=0.3$, $c_d=0$, $\gamma_C=14.4$, and $\gamma_F=12.5$.

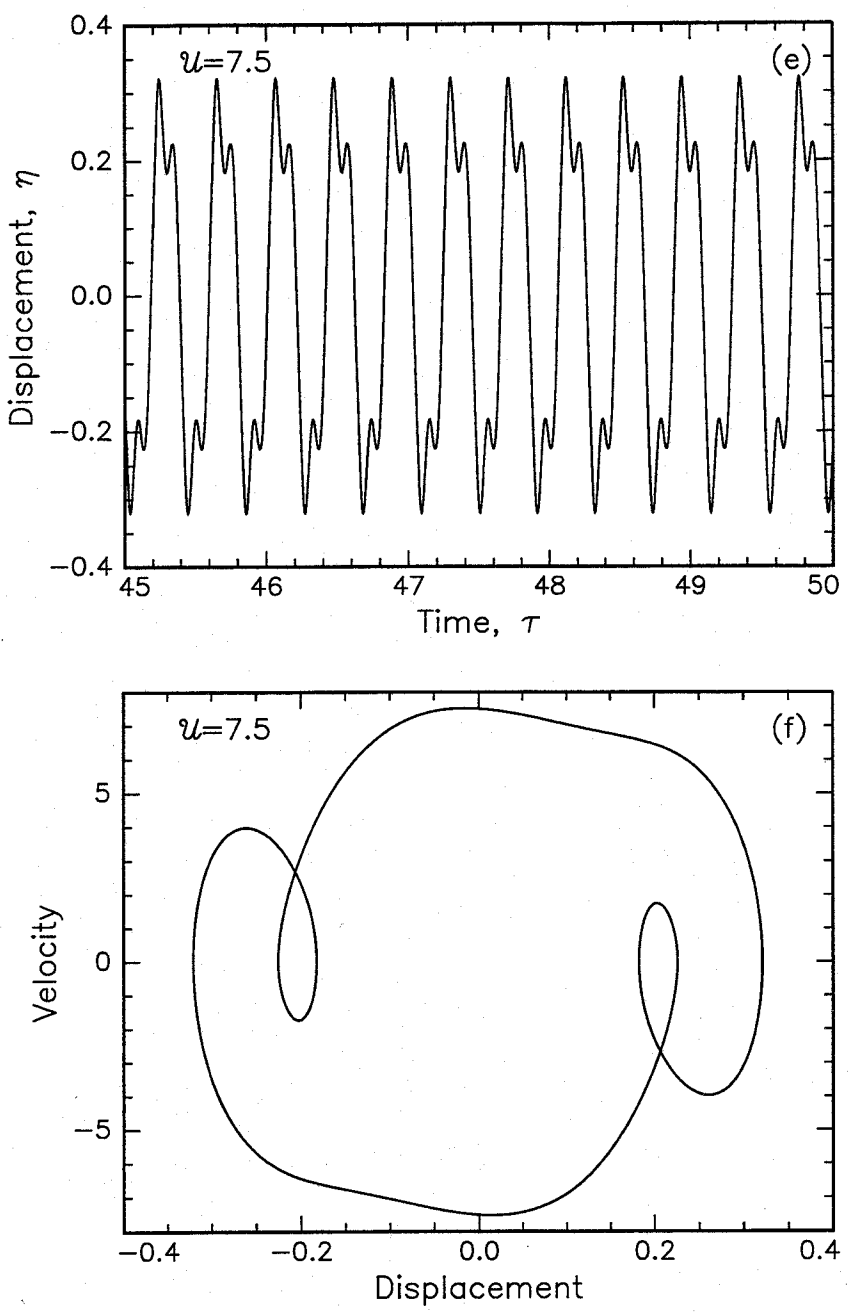


Figure 11: (e) Displacement-versus-time diagram and (f) phase portrait diagram for $\mathscr{U}=7.5$; the parameters are set at f=0.7, $\beta=0.47$, $\varepsilon \, c_f=0.5$, $\chi=1$, h=0, $\chi_e=0.00667$, $\overline{\chi}_e=0.00785$, $c_b=0.3$, $c_d=0$, $\gamma_C=14.4$, and $\gamma_F=12.5$.

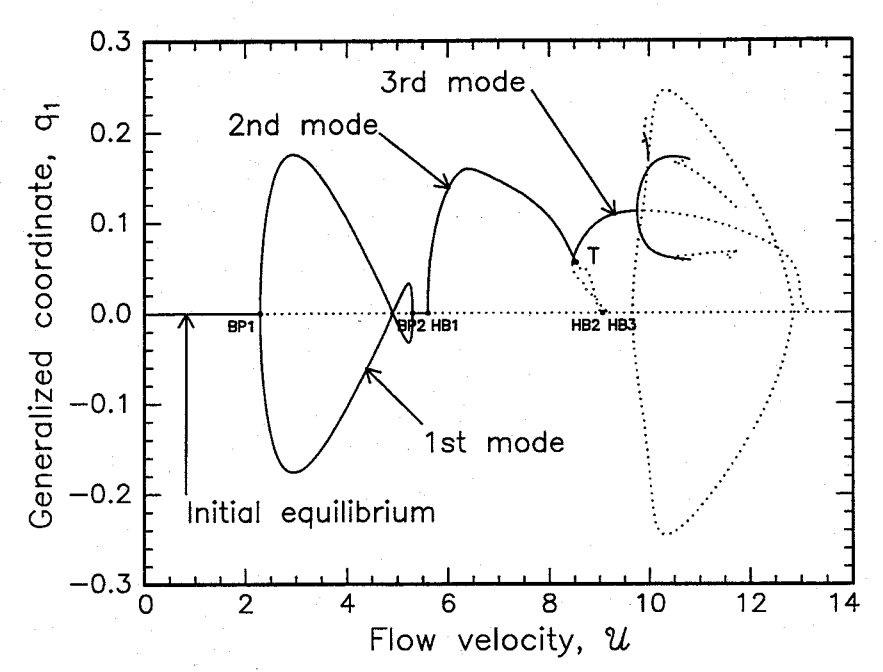


Figure 12: Bifurcation diagram for f=0.7, $\beta=0.47$, $\varepsilon c_f=0.5$, $\chi=1$, h=0, $\chi_e=0.00667$, $\overline{\chi}_e=0.00785$, $c_b=0.3$, $c_d=0$, $\gamma_c=14.4$, and $\gamma_F=12.5$, using a 5-mode Galerkin approximation, showing the first generalized co-ordinate versus \mathscr{U} : —————, stable solution;, unstable solution.

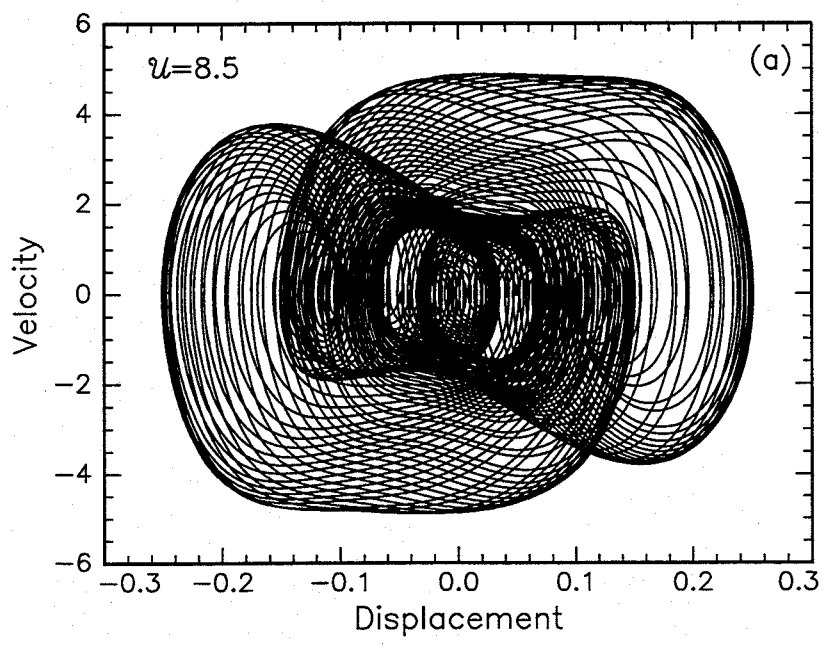


Figure 13: (a) Phase portrait diagram for $\mathscr{U}=8.5$; the parameters are set at f=0.7, $\beta=0.47$, $\varepsilon c_f=0.5$, $\chi=1$, h=0, $\chi_e=0.00667$, $\overline{\chi}_e=0.00785$, $c_b=0.3$, $c_d=0$, $\gamma_C=14.4$, and $\gamma_F=12.5$.

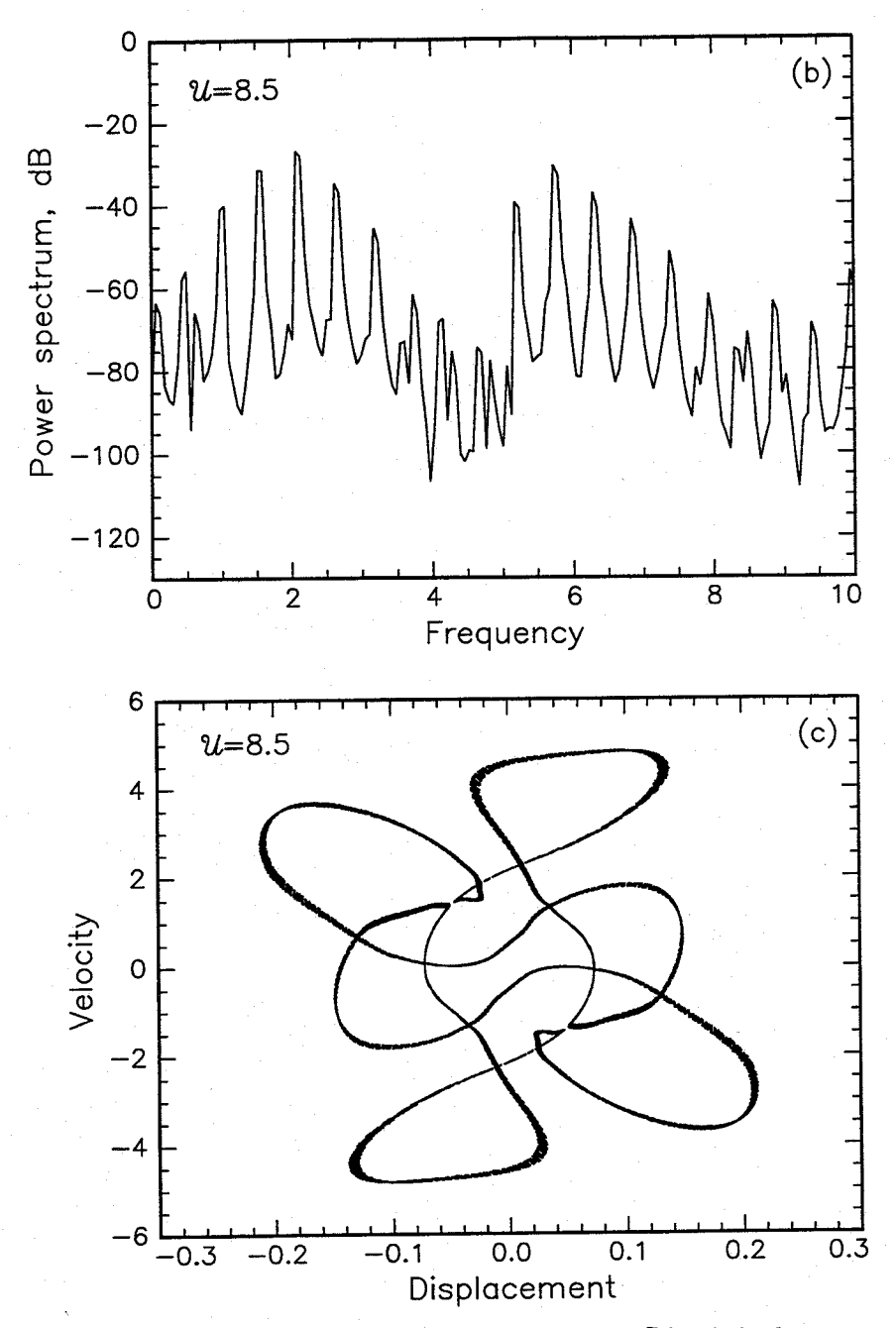


Figure 13: (b) Power spectrum and (c) Poincaré section for $\mathscr{U}=8.5$; the parameters are set at f=0.7, $\beta=0.47$, $\varepsilon c_f=0.5$, $\chi=1$, h=0, $\chi_e=0.00667$, $\overline{\chi}_e=0.00785$, $c_b=0.3$, $c_d=0$, $\gamma_C=14.4$, and $\gamma_F=12.5$.

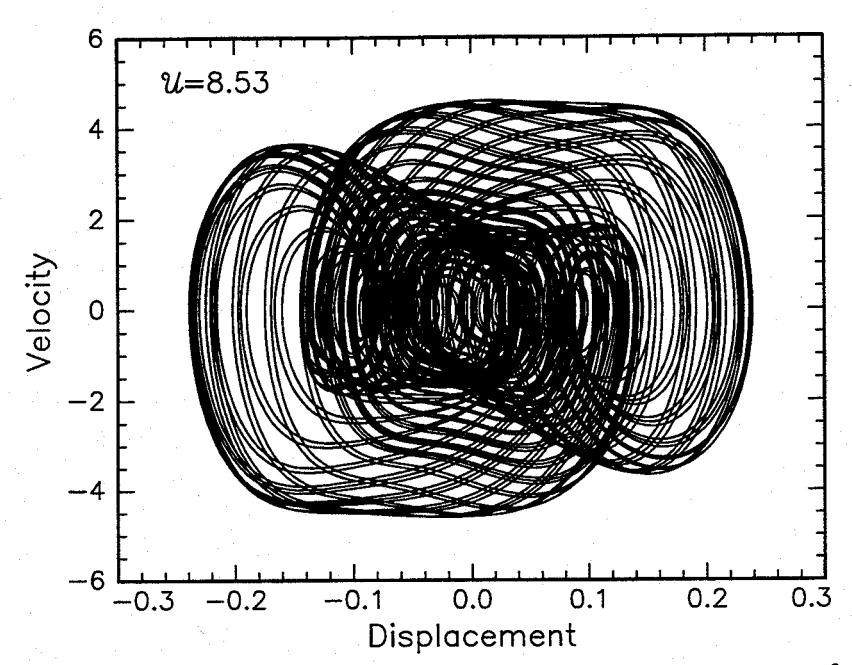


Figure 14: Phase portrait diagram for $\mathscr{U}=8.529$; the parameters are set at f=0.7, $\beta=0.47$, $\varepsilon c_f=0.5$, $\chi=1$, h=0, $\chi_e=0.00667$, $\overline{\chi}_e=0.00785$, $c_b=0.3$, $c_d=0$, $\gamma_C=14.4$, and $\gamma_F=12.5$.

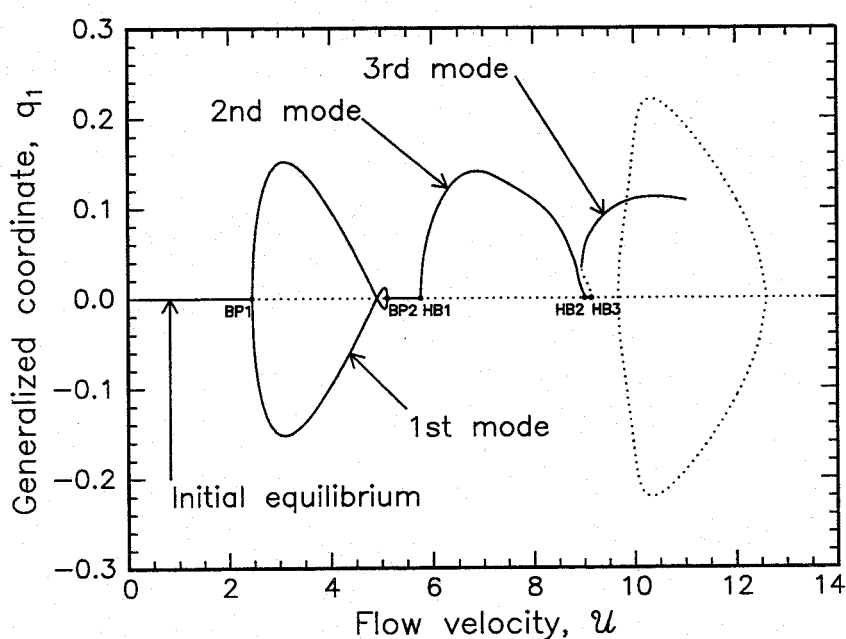


Figure 15: Bifurcation diagram for f = 0.6, $\beta = 0.47$, $\varepsilon c_f = 0.25$, $\chi = 1$, h = 0, $\chi_e = 0.00667$, $\overline{\chi}_e = 0.00785$, $c_b = 0.4$, $c_d = 0$, $\gamma_c = 14.4$, and $\gamma_F = 12.5$, using a 5-mode Galerkin approximation, showing the first generalized co-ordinate versus \mathscr{U} : ————, stable solution;, unstable solution.

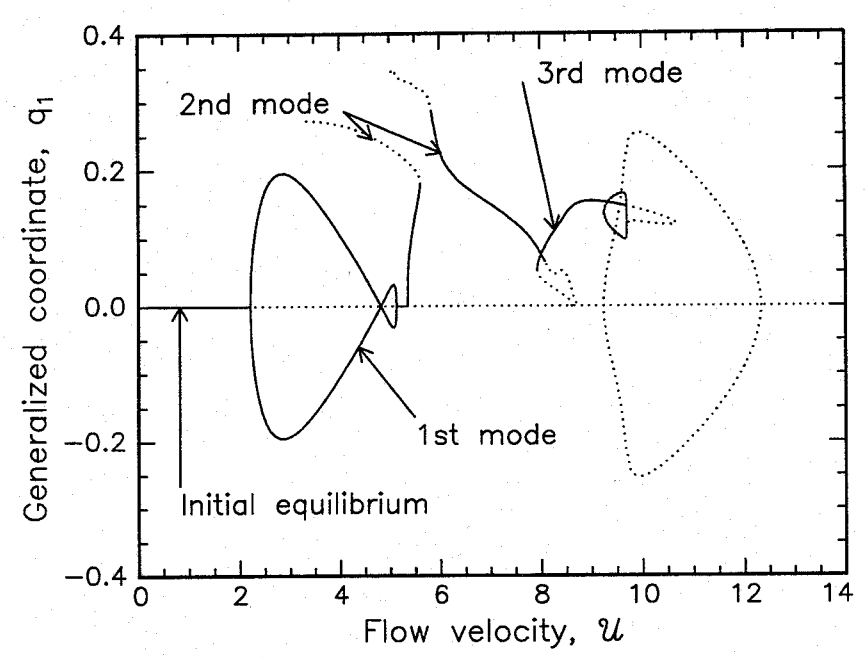


Figure 16: Bifurcation diagram for f = 0.7, $\beta = 0.47$, $\varepsilon c_f = 0.25$, $\chi = 1$, h = 0, $\chi_e = 0.00667$, $\overline{\chi}_e = 0.00785$, $c_b = 0.3$, $c_d = 0$, $\gamma_c = 14.4$, and $\gamma_F = 12.5$, using a 5-mode Galerkin approximation, showing the first generalized co-ordinate versus \mathscr{U} : ————, stable solution;, unstable solution.

APPENDIX A: METHODS TO ACCOUNT FOR TAPERING-END BOUNDARY CONDITIONS

Two different methods are presented and developed in order to obtain the eigenfunctions and to analyze the stability of a cantilevered cylinder with a tapering end in axial flow. Since the boundary conditions are not as simple as when considering a cantilevered cylinder with no endpiece, we shall present in detail two methods suitable to take them into account.

6.1 A.1 PRESENTATION OF THE PROBLEM

The equation of motion of the cantilevered cylinder as derived in [1] is of third-order magnitude and hence nonlinear; furthermore, the boundary conditions are time- and flow velocity-dependent.

Let us write for simplicity the equation of motion in the form $F(\eta, \mathcal{U}) = 0$, where η is the dimensionless displacement and \mathcal{U} the flow velocity parameter. Then, with the boundary conditions added, the boundary value problem may be formulated as

$$F(\eta(\xi,\tau),\mathcal{U}) = 0,$$

$$\eta(0,\tau) = \eta'(0,\tau) = 0, \ \eta''(1,\tau) = -\eta'''(1,\tau) + B(\eta(1,\tau),\mathcal{U}) = 0,$$
(A.1)

(A.2)

where $B(\eta, \mathcal{U})$ represents a complementary term in the end-shear boundary condition due to the tapering end. An alternative way of formulating the problem is the following:

$$F(\eta(\xi,\tau),\mathcal{U}) + \delta(\xi-1)B(\eta(\xi,\tau),\mathcal{U}) = 0,$$

48

$$\eta(0,\tau) = \eta'(0,\tau) = 0, \quad \eta''(1,\tau) = \eta'''(1,\tau) = 0,$$
(A.3)

(A.4)

where $\delta(\xi-1)$ is the Dirac delta function. With these two formulations in mind, three methods may be proposed to decouple the equations, as follows.

Method (a) consists of utilizing the eigenfunctions $\Phi_j(\xi)$ of the problem $\eta'''' + \ddot{\eta} = 0$, i.e., the dry cantilevered-cylinder equation of motion, subject to boundary conditions (A.2) to discretize the system and apply them to the problem (A.1). In Method (b), the same eigenfunctions $\Phi_j(\xi)$ are used, but they are applied to an 'expanded domain' of the problem, which effectively means that the time-dependent boundary condition, i.e. the last of (A.2), is added to the equation of motion, i.e., the expression $\left[-\eta'''(1,\tau) + B(\eta(1,\tau),\mathcal{U})\right]$ is added to the left-hand side of (A.1) via a Dirac delta function. Finally, in Method (c), the cantilever beam eigenfunctions $\phi_j(\xi)$ satisfying (A.4) are used directly to decouple equation (A.3).

In the following we shall put the emphasis on the development of *Methods* (b) and (c) which for time-dependent boundary conditions give more accurate results than *Method* (a) (see Païdoussis [4], Section 4.6.2), which, henceforth, will not be discussed here.

6.1.1.1.1 A.2 DEVELOPMENT OF THE METHODS

6.1.1.1.1.1 A.2.1 GENERAL CONSIDERATIONS

Making use of the Ritz-Galerkin method in order to decouple the problem, we shall assume the non-dimensional displacement to be of the form

$$\eta(\xi, \tau) = \sum_{j=1}^{\infty} \Phi_j(\xi) q_j(\tau),$$

(A.5)

where $\Phi_j(\xi)$ are said to be comparison functions and satisfy both geometric and natural boundary conditions.

Considering the problem at hand and the non-dimensional parameters introduced for time, space, etc. [1], the equation of motion of a dry cantilevered beam is of the form

$$\eta'''' + \ddot{\eta} = 0.$$

(A.6)

Then, introducing $\eta_j(\xi,\tau) = \Phi_j(\xi) h_j(\tau)$ and assuming the time function to be of the form $h_j(\tau) = h_j^0 e^{\lambda_j \tau}$ thus satisfying $\dot{h}_j(\tau) = \lambda_j h_j(\tau)$, where λ_j is a complex eigenvalue, equation (A.6) gives

$$\Phi_{j}^{""} h_{j} + \lambda_{j}^{2} \Phi_{j} h_{j} = 0,$$

$$\Rightarrow \Phi_{j}^{""} + \lambda_{j}^{2} \Phi_{j} = 0,$$

$$\Rightarrow \Phi_{j}^{""} - \Lambda_{j}^{4} \Phi_{j} = 0,$$

(A.7)

where $\Lambda_j^4 = -\lambda_j^2$, and Λ_j is a complex dimensionless eigenvalue. We notice that four different eigenvalues Λ_j , namely Λ_j , $-\Lambda_j$, $i\Lambda_j$, $-i\Lambda_j$, are possible. This is due to the fact that the differential equation is linear and of fourth-order and so that its solution can be written in terms of four independent functions. Hence, the modal shape $\Phi_j(\xi)$ can be written in the form

$$\Phi_{j}(\xi) = a_{j} \cos(\Lambda_{j} \xi) + b_{j} \sin(\Lambda_{j} \xi) + c_{j} \cosh(\Lambda_{j} \xi) + d_{j} \sinh(\Lambda_{j} \xi), \quad j = 1, \dots \infty.$$

(A.8)

Then, the next step is to determine these four coefficients by making use of the complete boundary conditions, equation (6). Actually, since Λ_j is also unknown, a fifth equation is required, taken to be a normalizing condition. Thus, the mode shape of this freely vibrating beam should also satisfy $\int_0^1 \Phi_i(\xi) \, d\xi = \delta_{ij}$, where δ_{ij} represents Kronecker delta function.

We see that these five constants generally depend on the boundary conditions, and hence on the flow velocity \mathcal{U} . Furthermore, concerning Λ_j , some problems may arise when introducing time-dependent boundary conditions as will be studied later (Section A.2.4).

In what follows, in Sections A.2.2, A.2.3 and A.2.4, we present the analysis for determining appropriate comparison functions, i.e. solutions to the dry-beam equation, subject to whatever boundary conditions are appropriate for either Method(b) or Method(c). For sake of clarity we shall begin with Method(c).

The solution of the full problem of a cylinder subject to axial flow is presented in Section A.3.

A.2.2 METHOD (c)

In this case, the equation to be solved is the Euler-Bernoulli beam equation, equation (A.6), subject to the classical cantilevered beam boundary conditions,

$$\begin{cases} \phi_j = \phi'_j = 0 & \text{at} \quad \xi = 0, \\ \phi''_j = \phi'''_j = 0 & \text{at} \quad \xi = 1. \end{cases}$$

(A.9)

After some manipulations, we obtain the characteristic equation $\cos \Lambda_j \cosh \Lambda_j + 1 = 0$, with eigenvalues $\Lambda_1 = 1.875$, $\Lambda_2 = 4.694$, etc. [10], and eigenfunctions

$$\phi_{j}(\xi) = (\cosh(\Lambda_{j}\xi) - \cos(\Lambda_{j}\xi)) - \sigma_{j}(\sinh(\Lambda_{j}\xi) - \sin(\Lambda_{j}\xi)),$$

(A.10)

where $\sigma_j = (\cos \Lambda_j + \cosh \Lambda_j)/(\sin \Lambda_j + \sinh \Lambda_j)$. In this method the eigenvalues Λ_j and the eigenfunctions ϕ_j are not dependent on system parameters (e.g., they do not change with the flow velocity), and need thus to be computed only once.

Then, expressing the solution as in (A.5) and truncating it to the first N comparison functions (say N=8), substituting it into equation (A.3), pre-multiplying by ϕ_i , and integrating over the interval [0,1] in order to use the orthogonality of the beam modes, we obtain the resulting equation of motion in terms of the generalized coordinates, which takes the complementary term of the tapering-end boundary condition into account.

Before proceeding any further and presenting the comparison functions to be used in *Method (b)* in detail, let us first consider a special, simplified form of *Method (b)* in which the coefficients involving time dependency are set to zero in which case real eigenvalues are obtained.

6.1.1.1.1.2 A.2.3 SPECIAL, SIMPLIFIED FORM OF METHOD (b)

The comparison functions used in Method (b) are the eigenfunctions of the dry beam equation, equation (A.6), subject to the actual boundary conditions (i.e., the boundary conditions for a cylinder in axial flow). These boundary conditions are functions of \mathcal{U} (and other parameters), and hence so will be the comparison functions and the eigenvalues Λ_j . For simplicity, let us first examine the time-independent boundary conditions:

$$\begin{cases} -\eta_{j}^{\prime\prime\prime} - \left(\frac{1}{2} \overline{\chi}_{e} \varepsilon c_{f} - \chi f\right) \mathcal{U}^{2} \eta_{j}^{\prime} + \left(\frac{1}{2} \mathcal{U}^{2} \varepsilon c_{f} h + \gamma_{C} - \gamma_{F}\right) \chi_{e} \eta_{j}^{\prime} = \eta_{j}^{\prime\prime} = 0 & \text{at } \xi = 1, \\ \eta_{j} = \eta_{j}^{\prime} = 0 & \text{at } \xi = 0. \end{cases}$$

(A.11)

Then, substituting $\eta_j(\xi,\tau)$ by $\Phi_j(\xi)h_j(\tau)$ into (A.11), and considering a modal shape expression of the form (A.8), we obtain after some simplifications the following system of equation:

$$\begin{aligned} &a_{j} \Big[\cos \Lambda_{j} + \cosh \Lambda_{j} \Big] + b_{j} \Big[\sin \Lambda_{j} + \sinh \Lambda_{j} \Big] = 0, \\ &a_{j} \Big[-\Lambda_{j}^{3} \Big(\sin \Lambda_{j} - \sinh \Lambda_{j} \Big) + \\ &\Lambda_{j} \Big(\Big(\frac{1}{2} \overline{\chi}_{e} \varepsilon c_{f} - \chi f \Big) \mathcal{U}^{2} + \Big(\frac{1}{2} \mathcal{U}^{2} \varepsilon c_{f} h + \gamma_{c} - \gamma_{F} \Big) \chi_{e} \Big) \left(-\sin \Lambda_{j} - \sinh \Lambda_{j} \right) \Big] \\ &+ b_{j} \Big[-\Lambda_{j}^{3} \Big(-\cos \Lambda_{j} - \cosh \Lambda_{j} \Big) + \\ &\Lambda_{j} \Big(\Big(\frac{1}{2} \overline{\chi}_{e} \varepsilon c_{f} - \chi f \Big) \mathcal{U}^{2} + \Big(\frac{1}{2} \mathcal{U}^{2} \varepsilon c_{f} h + \gamma_{c} - \gamma_{F} \Big) \chi_{e} \Big) \left(\cos \Lambda_{j} - \cosh \Lambda_{j} \right) \Big] = 0, \end{aligned}$$

(A.12)

where the unknowns, which are real, are a_j , b_j , and Λ_j [$c_j = -a_j$ and $d_j = -b_j$].

For non-trivial solutions, the associated determinant (i.e., the characteristic equation) must be zero. So, we seek eigenvalues Λ_j that give a null determinant. We notice that the eigenvalues depend on several physical parameters. Here, all parameters $(f,\chi,h,\,\epsilon\,c_f\,,\,\chi_e,\,\overline{\chi}_e,\,\gamma_C$ and $\gamma_F)$ are fixed except the flow velocity $\mathcal U$, leading to eigenvalues that are $\mathcal U$ -dependent.

For f=0.8, $\chi=1$, h=0, $\varepsilon c_f=1$, $\chi_e=0.00667$, $\overline{\chi}_e=0.00785$ and $\gamma_C=\gamma_F=0$ the evolution of the 1st and 2nd eigenvalue with respect to the fluid velocity $\mathcal U$ is shown in Figure A.1(a-b).

We notice that for U = 0 both eigenvalues are close to those of a dry beam subject to the classical cantilevered beam boundary conditions (see Section A.2.2). However, with increasing

 ${\cal U}$, it appears that the 1st eigenvalue behaves in a peculiar manner. In fact, all eigenvalues except the 1st seem to converge to a non-null fixed value when increasing the flow velocity; for instance, the 2nd eigenvalue decreases from 4.6 to 3.2 approximately and appears to level out as ${\cal U}$ is increased to ${\cal U}\sim 20$. In contrast, the 1st eigenvalue converges abruptly to zero for ${\cal U}\sim 1.58$, and then, remains equal to zero when increasing ${\cal U}$ further.

Before closing this section, we should add that the phenomenon mentioned above *seems* to predict buckling instability for the dry cantilevered cylinder with wet boundary conditions, i.e., the cylinder may diverge for $\mathcal{U} \sim 1.58$. This observation is of particular interest since buckling is found to occur at $\mathcal{U} \sim 2.05$ (a definitely higher flow velocity) as will be seen in Section A.3.2 when studying the complete problem of the cylinder immersed in an axial steady flow with tapering-end boundary conditions. However, we notice that this simple system, a dry beam with wet boundary conditions, is close to the complete system, at least as far as first-mode divergence is concerned.

A.2.4 METHOD (b)

Method (b) is now examined in its general form in order to confirm these results. The time-dependent terms are replaced in the boundary condition leading then to complex eigenvalues.

Here, we have a more intricate situation since the eigenvalues are not only velocity-dependent but also time dependent. In this case, the equation of motion is again (A.6), and the boundary conditions are of the form

$$\begin{cases} -\eta_{j}^{"''} + \left(1 + (\chi f - 1)\beta\right)\chi_{e} \ddot{\eta}_{j} + \left(\frac{1}{2}\overline{\chi}_{e}\varepsilon c_{f} - \chi f\right)\mathcal{U}\sqrt{\beta}\dot{\eta}_{j} - \chi f\mathcal{U}^{2}\eta_{j}^{\prime} \\ + \chi f\mathcal{U}\sqrt{\beta}\chi_{e}\dot{\eta}_{j}^{\prime} + \left(\frac{1}{2}\mathcal{U}^{2}\varepsilon c_{f}\left(h\chi_{e} + \overline{\chi}_{e}\right) + (\gamma_{C} - \gamma_{F})\chi_{e}\right)\eta_{j}^{\prime} = \eta_{j}^{"} = 0 \text{ at } \xi = 1, \\ \eta_{j} = \eta_{j}^{\prime} = 0 \text{ at } \xi = 0. \end{cases}$$

(A.13)

Substituting $\eta_j(\xi,\tau)$ by $\Phi_j(\xi)h_j(\tau)$ in (A.13) and assuming as in Section A.2.1 a time function evolution of the form $h_j(\tau) = h_j^0 e^{\lambda_j \tau}$, we finally obtain the following boundary conditions

$$\begin{cases} -\Phi_{j}^{"'} + \left(1 + (\chi f - 1)\beta\right)\chi_{e} \lambda_{j}^{2} \Phi_{j} + \left(\frac{1}{2}\overline{\chi}_{e} \varepsilon c_{f} - \chi f\right)\mathcal{U} \sqrt{\beta} \lambda_{j} \Phi_{j} - \chi f \mathcal{U}^{2} \Phi_{j}^{\prime} \\ + \chi f \mathcal{U} \sqrt{\beta} \chi_{e} \lambda_{j} \Phi_{j}^{\prime} + \left(\frac{1}{2}\mathcal{U}^{2} \varepsilon c_{f} \left(h \chi_{e} + \overline{\chi}_{e}\right) + (\gamma_{C} - \gamma_{F})\chi_{e}\right)\Phi_{j}^{\prime} = \Phi_{j}^{"} = 0 \quad \text{at} \quad \xi = 1, \\ \Phi_{j} = \Phi_{j}^{\prime} = 0 \quad \text{at} \quad \xi = 0. \end{cases}$$

(A.14)

Then, considering a modal shape expression of the form (A.8), we obtain after some manipulations the following system:

$$\begin{bmatrix}
a_{j} \left[\cos \Lambda_{j} + \cosh \Lambda_{j}\right] + b_{j} \left[\sin \Lambda_{j} + \sinh \Lambda_{j}\right] = 0, \\
a_{j} \left[-\Lambda_{j}^{3} \left(\sin \Lambda_{j} - \sinh \Lambda_{j}\right) + \left(-\left(1 + (\chi f - 1)\beta\right)\chi_{e} \lambda_{j}^{2} + \left(\frac{1}{2}\overline{\chi}_{e} \varepsilon c_{f} - \chi f\right)\mathcal{U}\sqrt{\beta} \lambda_{j}\right) \left(\cos \Lambda_{j} - \cosh \Lambda_{j}\right) \\
+ \Lambda_{j} \left(-\chi f \mathcal{U}^{2} + \chi f \mathcal{U}\sqrt{\beta} \chi_{e} \lambda_{j} + \frac{1}{2}\mathcal{U}^{2}\varepsilon c_{f} \left(h\chi_{e} + \overline{\chi}_{e}\right) + (\gamma_{C} - \gamma_{F})\chi_{e}\right) \left(-\sin \Lambda_{j} - \sinh \Lambda_{j}\right)\right] \\
+ b_{j} \left[-\Lambda_{j}^{3} \left(-\cos \Lambda_{j} - \cosh \Lambda_{j}\right) + \left(-\left(1 + (\chi f - 1)\beta\right)\chi_{e} \lambda_{j}^{2} + \left(\frac{1}{2}\overline{\chi}_{e} \varepsilon c_{f} - \chi f\right)\mathcal{U}\sqrt{\beta} \lambda_{j}\right) \left(\sin \Lambda_{j} - \sinh \Lambda_{j}\right) + \left(-\chi f \mathcal{U}^{2} + \chi f \mathcal{U}\sqrt{\beta}\chi_{e}\lambda_{j} + \frac{1}{2}\mathcal{U}^{2}\varepsilon c_{f} \left(h\chi_{e} + \overline{\chi}_{e}\right) + (\gamma_{C} - \gamma_{F})\chi_{e}\right) \left(\cos \Lambda_{j} - \cosh \Lambda_{j}\right)\right] = 0.$$
(A.15)

Here, we notice the presence of the eigenfrequency λ_j (we shall recall that $\Lambda_j^4 = -\lambda_j^2$). Hence, the equations can either be written in frequency or eigenvalue form, even if the latter one is easier.

Again, for non-trivial solutions we look for eigenvalues Λ_j or frequencies λ_j that give a null determinant to this system. This is a transcendental system equation with two possible solutions λ_j and $\overline{\lambda}_j$, each leading to four possible eigenvalues Λ_j ; hence, we obtain eight possible eigenvalues Λ_j , $-\Lambda_j$, $i\Lambda_j$, $-i\Lambda_j$ and their conjugates. According to the statement below equation (A.7), the solutions to the transcendental equation can then be written in terms of eight independent functions. Hence, we obtain two possible eigenfunctions, i.e., the mode shape $\Phi_j(\xi)$ and its conjugate $\overline{\Phi}_j(\xi)$.

This complex solution finally leads to a non-dimensional displacement of the form

$$\eta(\xi,\tau) = \sum_{j=1}^{\infty} (\Phi_{j}(\xi)h_{j}(\tau) + \overline{\Phi}_{j}(\xi)\overline{h}_{j}(\tau)).$$

For f = 0.8, $\beta = 0.5$, $\chi = 1$, h = 0, $\varepsilon c_f = 1$, $\chi_e = 0.00667$, $\overline{\chi}_e = 0.00785$ and $\gamma_C = \gamma_F = 0$ we have solved the system (A.15) for increasing values of the flow velocity \mathcal{U} . Moreover, since the eigenvalues are now complex we need to observe both real and imaginary parts. In what follows, we will essentially focus on the first eigenvalue in order to shed light on its behavior.

6.1.1.1.1.3 A.2.4.1 Evolution of the eigenvalues

To overcome numerical problems while solving the system (A.15), we used two different routines in order to find the roots of the eigenvalue problem. We first began using *Müller's* method, which is part of the IMSL Library software package. Then, we found some peculiar

problems regarding the first eigenvalue when increasing the fluid-velocity increment $\delta \mathcal{U}$, whereas no problem occurred with the other eigenvalues. Therefore, we also used the *secant* method in order to make some comparisons.

In the light of Figure A.2 which shows the real part of Λ_1 versus \mathcal{U} for the *secant* method and *Müller*'s method, we notice that something occurs for $\mathcal{U} \sim 1.27$: the first method predicts convergence of Λ_1 to zero for $\mathcal{U} \sim 1.58$ (implying instability (buckling) for the *dry* cantilevered cylinder with wet boundary conditions), whereas the second method seems to predict divergence to infinity of the first eigenvalue after $\mathcal{U} \sim 1.27$. Hence, the *secant* method is in complete agreement with the conclusions in Section A.2.3.

The only way to render these discrepancies a little more comprehensible is to consider also the evolution of the imaginary part of the first eigenvalue. However, before doing so, we should note that there is a singular point in both cases at $\mathcal{U} \sim 1.27$ (in principle, this could be responsible for some numerical problems, but it is not the case). However, when investigating the imaginary part versus the real part (which is not presented here for sake of brevity), we find that for both methods and for $\mathcal{U} \geq 1.27$, $\text{Re}(\Lambda_1) = \text{Im}(\Lambda_1)$. Even if at first sight this does not provide a complete explanation of the discrepancy obtained through the two methods, it encourages us to proceed in this direction.

So, let us consider solutions of the form $\Lambda_1 = \Lambda(1+i)$ for the system (A.15), with Λ real, and $|\Lambda_1| = \Lambda \sqrt{2}$. We have of course $\text{Re}(\Lambda_1) = \text{Im}(\Lambda_1)$. The aim is to verify if such solution does really exist and, if it does, what happens when increasing $\mathcal U$.

Figure A.3 shows the evolution of the real part of the determinant of the system (A.15) (which in fact is the exact opposite in sign to the imaginary part) versus Λ for two values of $\mathcal U$.

It can be concluded that there is no such solution for $\mathcal{U} \leq 1.27$. The first solution of that kind occurs for $\mathcal{U} \sim 1.27$ and is a double point. In fact, as \mathcal{U} is increased beyond 1.27, two solutions arise as can be observed for $\mathcal{U} \sim 1.3$. So, undoubtedly there are two kinds of solutions when increasing \mathcal{U} : we notice that the smallest one converges to zero whereas the largest one seems to diverge to infinity. Hence, it is understood that the *secant method* is able to find the first one (whatever the increment in \mathcal{U} is, up to 0.2, which should be large enough), whereas Müller's method finds the second one (at least for an increment in \mathcal{U} up to 0.05).

The numerical problem being clarified, we need to find the solution that ought to be kept in the analysis, if not both? Actually, we cannot keep the solution found by Müller's method leading to a 1st eigenvalue which diverges as \mathcal{U} increases. Physically, this solution does not make sense (even if mathematically it does exist), because when increasing \mathcal{U} the modulus of the 1st eigenvalue becomes larger than any expected higher eigenvalue. [Furthermore, solving the final linearized system of the cantilevered cylinder immersed in steady flow with this kind of eigenvalue would lead to suspicious results.] So, definitely, we should keep the solution found by the *secant method*.

A.2.4.2 Further discussion

The physical reason for the difficulties already discussed is now clear. A cantilevered cylinder subjected to flow over its tapering end only (whereas the cylindrical part remains "dry") develops divergence (buckling) at sufficiently high flow velocity; i.e., the axial flow over an inclined tapering end leads to a lift force, which eventually overcomes the flexural restoring force. Buckling being a static instability, the same behaviour is obtained, whether time-dependent terms are eliminated or retained in the boundary conditions.

Since buckling instability is predicted for the dry beam with the wet tapering-end boundary conditions, it is useful to study (say to verify) what happens when varying the parameter f (which is a measure of the departure from ideal slender-body, inviscid flow theory, arising from (i) the lateral flow not being truly two-dimensional across the tapered end-piece, and (ii) boundary layer effects). Thus, f = 1 represents the ideally slender case, while normally $0 \le f \le 1$: for f = 1 we have an ideally streamlined free end, and for f = 0 a blunt free end.

Let us now see what happens for a small value of f. Figure A.4 represents the real part of Λ_1 for f=0.01 (there is in fact no use to represent the imaginary part), and we notice that it is qualitatively similar to what was predicted when considering real eigenvalues (see Figure A.1(a)), i.e., the Λ_1 converges to zero abruptly. When decreasing f, we noticed from results not presented here that the convergence to zero becomes more and more abrupt, i.e., beyond a certain \mathcal{U} , Λ_1 reaches zero very precipitously. However, we also noticed that the velocity for buckling increases drastically, and actually, the buckling velocity tends to infinity when the parameter f decreases to zero.

Hence, if we consider the extreme situation with f = 0, i.e., a blunt free end, there will be no buckling instability for the dry cantilevered cylinder with wet boundary conditions. This is indeed obvious since setting f to 0 removes the only forces that can overcome the flexural restoring force. [This is in agreement with the experiments conducted by Païdoussis $et\ al.$ [8] for the cantilever immersed in steady axial flow].

Since we completely developed the two methods we proposed at the outset, it is time now to compare them in the process of finding the eigenvalues of the complete linearized system representing the cantilevered cylinder immersed in an axial flow.

6.1.1.1.2 A.3. COMPARISON BETWEEN THE TWO METHODS

6.1.1.1.2.1 A.3.1 INTRODUCTION TO THE LINEARIZED PROBLEM

Once we have found the eigenvalues Λ_j by either method, the comparison functions Φ_j to be used in the analysis of the cylinder in flow become obvious. So, it is then possible to discretize the nonlinear equation of the complete problem at hand, following step-by-step the Ritz-Galerkin procedure.

Attention is nevertheless required here since for Method (b) (as stated previously) the non-dimensional displacement is of the form (A.16) while for Method (c) it is of the form (A.5). So, the matrices will not be of the same order, even for the same number of comparison functions.

Furthermore, before proceeding any further, concerning Method(b) it happens that having $Re(\Lambda_1) = Im(\Lambda_1)$ for $\mathcal{U} \ge 1.27$ implies that there are no longer eight solutions as predicted in Section A.2.4 but only four, since $\Lambda_1 = i\overline{\Lambda}_1$, $-\Lambda_1 = -i\overline{\Lambda}_1$, $i\Lambda_1 = -\overline{\Lambda}_1$, $-i\Lambda_1 = \overline{\Lambda}_1$. Hence, in the end, we need to consider Φ_1 and $\overline{\Phi}_1$ for $\mathcal{U} \le 1.27$, and only Φ_1 for $\mathcal{U} \ge 1.27$ (i.e., when increasing \mathcal{U} the order of the matrices may also change, but only once!).

Finally, when the procedure of discretisation is complete we find by both methods an equation of the form of equation (10) with only one major difference being that the two methods lead to different matrices (since the comparison functions are different).

Considering now only the linearized part of equation (10), $M_{ij}\ddot{q}_j + C_{ij}\dot{q}_j + K_{ij}q_j = 0$, it is of interest to study the stability of the *real* system through Argand diagrams.

To this end, solutions of the form $q(\tau) = e^{\lambda \tau}$ are considered, λ being a complex dimensionless eigenvalue. If the real part of λ is negative, motions will be damped, while if $\text{Re}(\lambda) > 0$ motions will be amplified, i.e., they will be unstable.

The system to solve is as follows:

$$\dot{Y} = \begin{bmatrix} O & I \\ -M^{-1}K & -M^{-1}C \end{bmatrix} Y,$$

where $Y = \{q, \dot{q}\}^T$.

Here, we shall restrain ourselves to flow velocities for the onset of divergence in the first mode, the regaining of stability in the first mode, flutter in the second mode, flutter in the third mode and the regaining of stability in the second mode (in a range of velocities between 0 and 10), and then, compare the values obtained by the two methods.

6.1.1.1.2.2 A.3.2 RESULTS

The results are obtained for different modes in order to compare the critical flow velocities for the different phenomena mentioned above. The results are also compared to an eight-mode computation, which, whatever the method, should give fairly good accuracy.

The results are summed up in Table A.1 and they have been conducted for f=0.8, $\beta=0.5,\ \chi=1,\ h=0,\ \varepsilon\,c_f=1,\ \chi_e=0.00667,\ \overline{\chi}_e=0.00785,\ c_b=0\ \ {\rm and}\ \gamma_C=\gamma_F=0.$

We observe that *Method* (b) is more accurate since with two modes, almost all of the information is obtained, even flutter in the 3rd mode; furthermore, *Method* (c) requires at least four modes to obtain this 3rd mode flutter. Finally, with three modes *Method* (b) gives results very close to those with eight modes.

What renders Method (b) more powerful is of course the fact that, in obtaining the comparison functions, we already go part of the way to solving the problem completely, since for each flow velocity \mathcal{U} the comparison functions satisfy the true boundary conditions, and thus are closer to the eigenfunctions of the real system. Furthermore, what is here of interest is the presence of the added conjugate modes that enable this method to achieve greater accuracy faster.

Nevertheless, provided enough modes are used, Method(c) is also accurate, even if the comparison functions are not flow-velocity dependent.

In order to illustrate what happens for these two methods (and to have a broader view), we present the Argand diagram of the linearized problem with two modes and using both methods in Figure 5.

Comparing Figure 5(a) and Figure 5(b) (and restraining ourselves to one side of the imaginary axis) it is seen that Method(b) provides four branches for two modes whereas only two branches are obtained with Method(c). We also notice in Figure 5(a) that Method(b) is able to predict 1st mode buckling instability, the regaining of stability in the 1st mode, flutter in the 2nd mode, and also the regaining of stability in the 2nd mode, and moreover flutter in the 3rd mode. The last two phenomena are not found by Method(c) (see Figure 5(b)). Method(b) seems at least to be ahead of Method(c), in terms of convergence/accuracy, by one mode.

So, it has been proved that Method(b) is a powerful tool, which requires fewer modes to achieve extremely good accuracy, compared to Method(c). Nevertheless, if the number of modes is increased sufficiently, Method(c) also leads to very good results. In fact, this is the purpose of the Ritz-Galerkin method: provided enough modes are used, good accuracy should be reached sooner or later, whatever the form of the comparison functions chosen. So, we have here a dilemma: reaching better accuracy with good but fewer comparison functions and performing

long calculations (up to ten minutes for *Method* (b) for three modes), or using more comparison functions of inferior quality, but saving time in the calculations (almost instantaneous even for eight modes)?

6.2 A.4 CONCLUSION

Despite the fact that Method(b) is more accurate, we have throughout this work noticed that there are more problems to be circumvented when used this method, compared to Method(c). Furthermore, the time needed to perform calculations is likely to discourage anyone. This is especially true when solving nonlinear problems where fourth-order tensors that depend upon comparison functions need to be computed numerically. Therefore, unless computers increase their performance exponentially, Method(c) is to be recommended. However, attention is required as far as the number of comparison functions needed to reach the desired accuracy is concerned.

In the light of this work, the study of the nonlinear equation of the cylinder immersed in an axial flow will be undertaken using Method(c) exclusively.

7. TABLES

Table A.1: Critical flow velocities using *Method* (b) and (c) for a different number of modes.

	1 mode		2 modes		3 modes		8 modes
Instabilities	Method	Method	Method	Method	Method	Method	Both
	<i>(b)</i>	<i>(c)</i>	<i>(b)</i>	(c)	<i>(b)</i>	(c)	methods
1st mode	2.07	2.13	2.06	2.05	2.06	2.05	2.06
divergence							
1st mode			4.93	5.56	4.93	5.05	4.94
restability							
2nd mode			5.29	5.78	5.24	5.27	5.24
flutter							_
3rd mode			8.97		8.45		8.41
flutter							
2nd mode			8.95		8.62		8.64
restability							

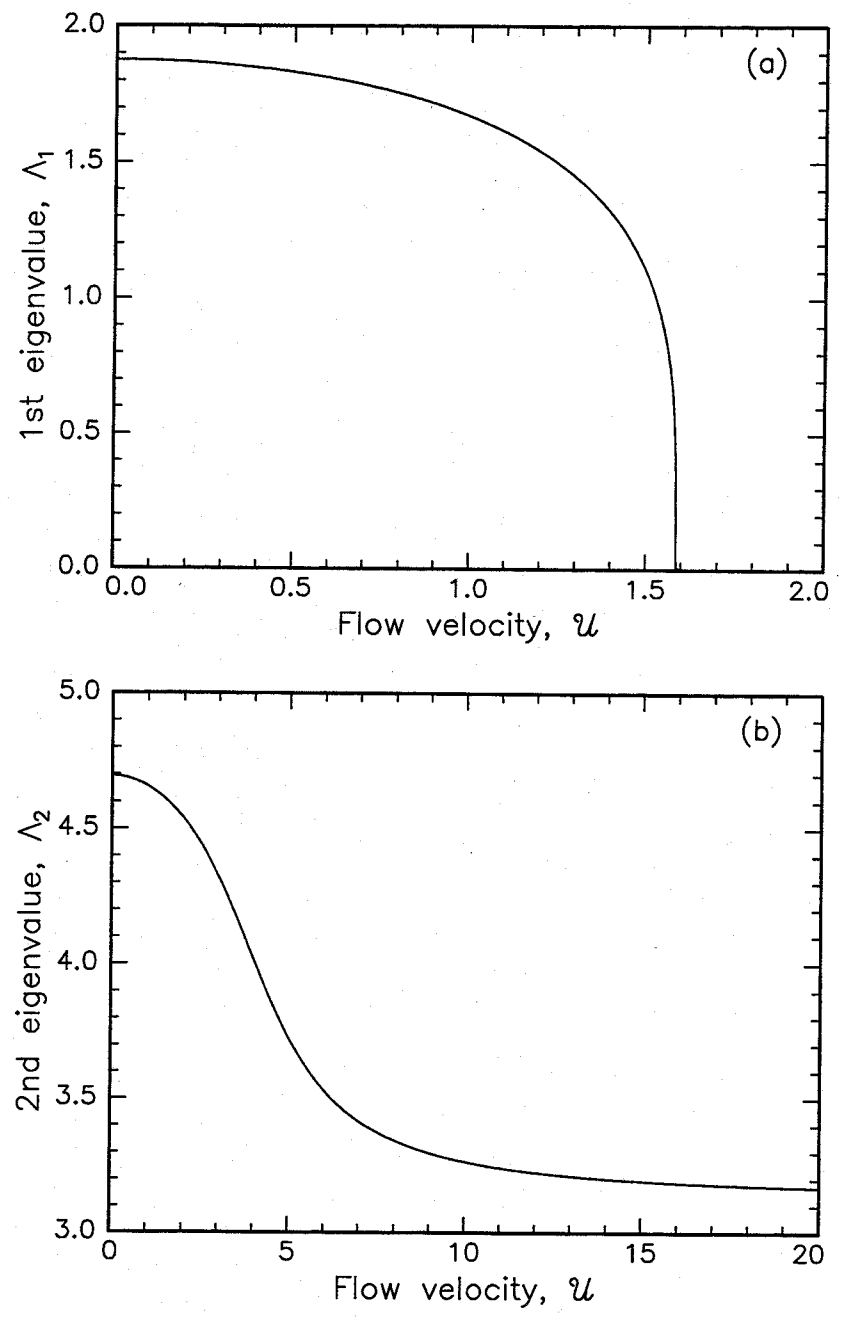


Figure A.1: Evolution of (a) the 1st eigenvalue and (b) the 2nd eigenvalue with the dimensionless flow velocity \mathscr{U} . The parameters are set at f=0.8, $\chi=1$, h=0, $\varepsilon c_f=1$, $\chi_\varepsilon=0.00667$, $\overline{\chi}_\varepsilon=0.00785$, and $\gamma_C=\gamma_F=0$.

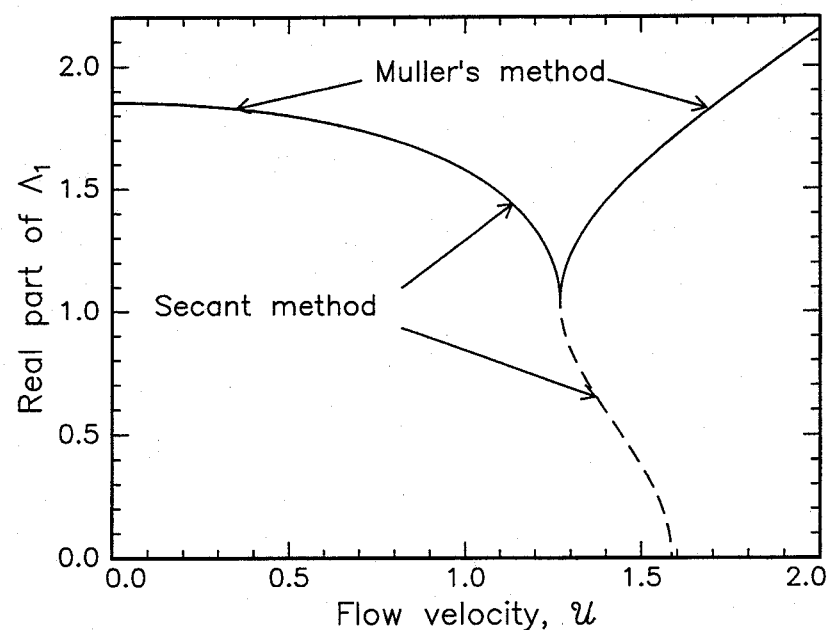


Figure A.2: Evolution of the real part of the 1st eigenvalue with the dimensionless flow velocity \mathscr{U} , using the *secant* method and Müller's method. The parameters are set at f=0.8, $\beta=0.5$, $\chi=1$, h=0, $\varepsilon c_f=1$, $\chi_e=0.00667$, $\overline{\chi}_e=0.00785$, and $\gamma_C=\gamma_F=0$.

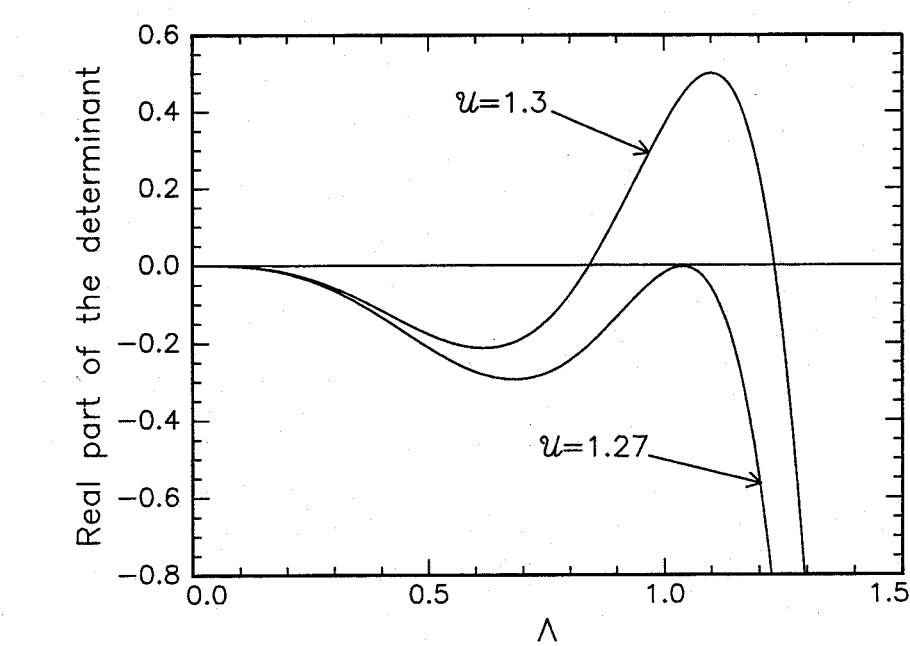
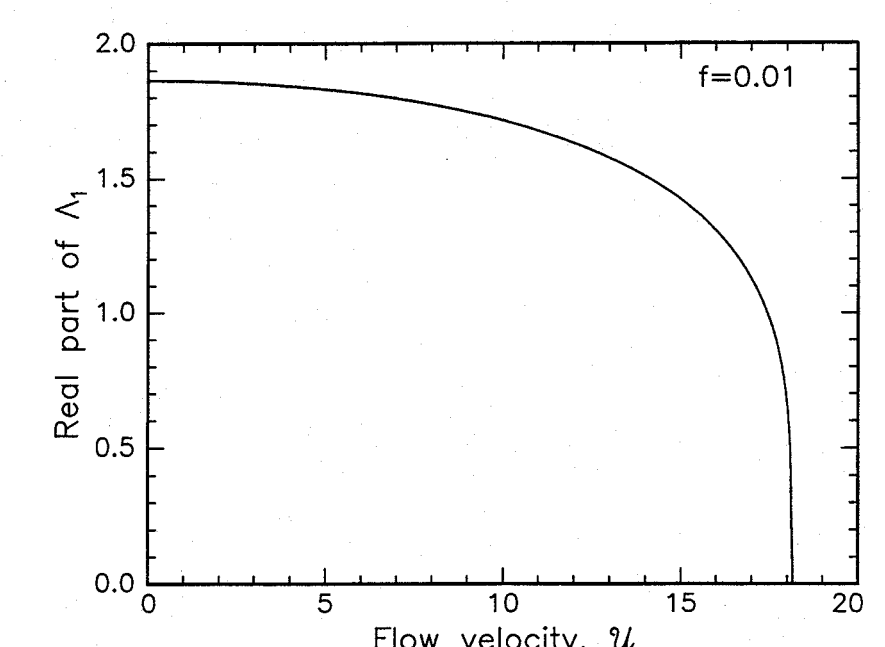


Figure A.3: Evolution of the real part of the determinant for the system (A.15) versus the modulus Λ for $\mathscr{U}=1.27$ and $\mathscr{U}=1.3$. The parameters are set at f=0.8, $\beta=0.5$, $\chi=1$, h=0, $\varepsilon c_f=1$, $\chi_e=0.00667$, $\overline{\chi}_e=0.00785$, and $\gamma_C=\gamma_F=0$.



Flow velocity, $\mathcal U$ Figure A.4: Evolution of the real part of the 1st eigenvalue versus the flow velocity $\mathcal U$, for f=0.01. The parameters are set at $\beta=0.5$, $\chi=1$, h=0, $\varepsilon c_f=1$, $\chi_e=0.00667$, $\overline{\chi}_e=0.00785$, and $\gamma_C=\gamma_F=0$.

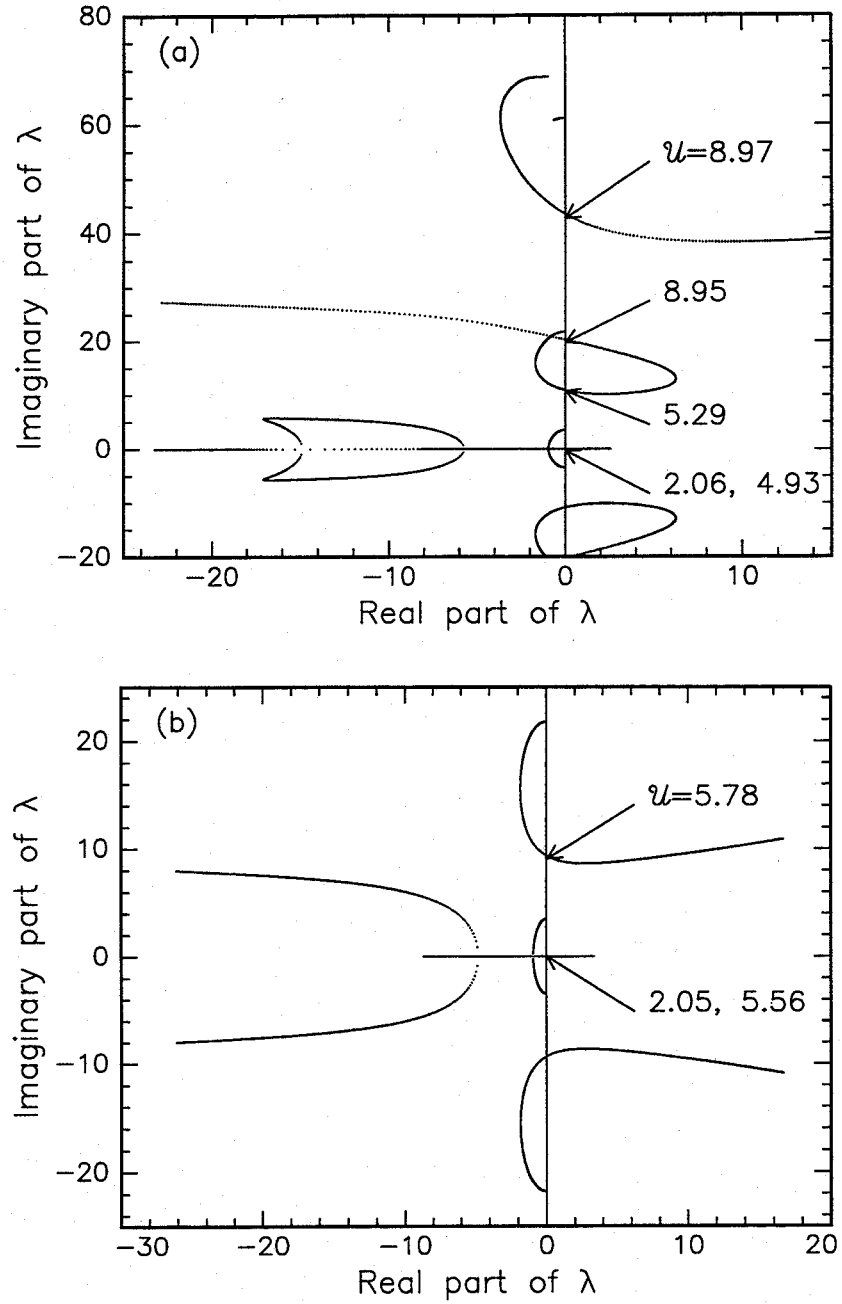


Figure A.5: Argand diagram obtained for two modes with (a) Method (b) and (b) Method (c) showing the dimensionless eigenvalues λ with flow velocity $\mathcal U$ as parameter. The other parameters are set at f=0.8, $\beta=0.5$, $\chi=1$, h=0, $\varepsilon c_f=1$, $\chi_e=0.00667$, $\overline{\chi}_e=0.00785$, $c_b=0$ and $\gamma_C=\gamma_F=0$.

APPENDIX B: MATRIX AND TENSOR COEFFICIENTS FOR THE INEXTENSIBLE CANTILEVERED CYLINDER

The equation of motion for the inextensible cantilevered cylinder is

$$\begin{aligned} M_{ij}\ddot{q}_{j} + C_{ij}\dot{q}_{j} + K_{ij}q_{j} + r_{ijk}q_{j}|q_{k}| + \overline{s}_{ijk}|q_{j}|\dot{q}_{k}| + \widetilde{s}_{ijk}q_{j}|\dot{q}_{k}| + t_{ijk}\dot{q}_{j}|\dot{q}_{k}| + \alpha_{ijkl}q_{j}q_{k}q_{l} \\ + \beta_{ijkl}q_{j}q_{k}\dot{q}_{l} + \gamma_{ijkl}q_{j}\dot{q}_{k}\dot{q}_{l} + \eta_{ijkl}\dot{q}_{j}\dot{q}_{k}\dot{q}_{k} + \mu_{ijkl}q_{j}q_{k}\ddot{q}_{l} = 0. \end{aligned}$$

The mass, damping and stiffness matrices are defined by

$$\begin{split} & M_{ij} = \left(1 + \left(\chi \, f - 1\right)\beta\right)\chi_{e}\,\phi_{i}\left(1\right)\phi_{j}\left(1\right) + \left(1 + \left(\chi - 1\right)\beta\right)\delta_{ij}\,, \\ & C_{ij} = \left(\frac{1}{2}\,\overline{\chi}_{e}\,\varepsilon\,c_{f} - \chi\,f\right)\mathcal{U}\,\sqrt{\beta}\,\phi_{i}(1)\phi_{j}(1) + \chi\,f\,\mathcal{U}\,\sqrt{\beta}\,\chi_{e}\,\phi_{i}(1)\phi_{j}'(1) + 2\,\chi\,\mathcal{U}\,\sqrt{\beta}\,b_{ij} + \frac{1}{2}\,\mathcal{U}\,\varepsilon\,c_{f}\,\sqrt{\beta}\,\delta_{ij}\,, \\ & K_{ij} = \left(\left(\gamma_{C} - \gamma_{F}\right)\chi_{e} + \frac{1}{2}\,\mathcal{U}^{2}\varepsilon\,c_{f}\left(\overline{\chi}_{e} + h\,\chi_{e}\right) - \chi\,f\,\mathcal{U}^{2}\right)\phi_{i}(1)\,\phi_{j}'(1) + \chi\,\mathcal{U}^{2}c_{ij} + \\ & \left(\gamma_{C} - \gamma_{F} + \frac{1}{2}\,\mathcal{U}^{2}\varepsilon\,c_{f}(1 + h)\right)\left(b_{ij} + d_{ij} - c_{ij}\right) + \lambda_{j}^{4}\delta_{ij} - \frac{1}{2}\,\mathcal{U}^{2}c_{b}\,c_{ij}\,; \end{split}$$

 δ_{ij} is Kronecker's delta, λ_j are the dimensionless eigenvalues of a cantilever beam and the constants, b_{ij} , c_{ij} , d_{ij} , introduced by Paidoussis & Issid (1974), are given by

$$b_{ij} = \int_0^1 \phi_i \, \phi'_j \, d\xi, \quad c_{ij} = \int_0^1 \phi_i \, \phi''_j \, d\xi, \quad d_{ij} = \int_0^1 \xi \, \phi_i \, \phi''_j \, d\xi.$$

The coefficients α_{ijkl} , β_{ijkl} , χ_{ijkl} , γ_{ijkl} , η_{ijkl} , μ_{ijkl} , r_{ijk} , r_{ijk} , are computed numerically from the integrals of the eigenfunctions, $\phi_i(\xi)$; their definition is more complicated:

$$\begin{split} \boldsymbol{\beta}_{ijkl} &= \chi \, \boldsymbol{\mathcal{U}} \, \sqrt{\beta} \left\{ \frac{7}{2} \int_{0}^{1} \!\!\!\! \phi_{i} \, \phi_{j}' \, \phi_{k}' \, \phi_{l}' \, d\xi - \frac{3}{2} \int_{0}^{1} \!\!\!\! \phi_{i} \, \phi_{j}'' \, \phi_{k}' \, \phi_{l} \, d\xi - 2 \, \int_{0}^{1} \!\!\!\! \phi_{i} \, \phi_{j}'' \left(\int_{\xi}^{1} \!\!\!\! \phi_{k}' \, \phi_{l}' \, d\xi \right) d\xi \right\} \\ &+ 2 \int_{0}^{1} \!\!\!\! \phi_{i} \, \phi_{j}'' \left(\int_{0}^{\xi} \!\!\!\! \phi_{k}' \, \phi_{l}' \, d\xi \right) d\xi \right\} - \frac{1}{4} \, \boldsymbol{\mathcal{U}} \, \sqrt{\beta} \, \boldsymbol{\varepsilon} \, \boldsymbol{c}_{f} \int_{0}^{1} \!\!\!\! \phi_{i} \, \phi_{j}' \, \phi_{k}' \, \phi_{l} \, d\xi, \end{split}$$

$$\begin{split} \gamma_{ijkl} &= -\frac{3}{2} \, \chi \, \beta \int_0^1 \!\! \phi_i \phi_j' \phi_k \phi_l' \, \, d\xi - (1-\beta) \int_0^1 \!\! \phi_i \, \phi_j'' \left(\int_\xi^1 \!\! \int_0^\xi \!\! \phi_k' \, \phi_l' \, \, d\xi \, d\xi \right) d\xi \\ &\quad + \!\! \left(1 \! + \! \left(\chi \! - \! 1 \right) \!\! \beta \right) \!\! \int_0^1 \!\! \phi_i \, \phi_j' \! \left(\int_0^\xi \!\! \phi_k' \, \phi_l' \, \, d\xi \right) d\xi + 2 \, \chi \, \beta \int_0^1 \!\! \phi_i \, \phi_k' \! \left(\int_0^\xi \!\! \phi_j' \, \phi_l' \, \, d\xi \right) d\xi \\ &\quad - \frac{1}{2} \, \beta \, \varepsilon \, c_f \int_0^1 \!\! \phi_i \, \phi_k \! \left(\int_0^\xi \!\! \phi_j' \, \phi_l' \, \, d\xi \right) d\xi - \frac{1}{4} \, \beta \, \varepsilon \, c_f \int_0^1 \!\! \phi_i \phi_j' \phi_k \phi_l \, \, d\xi + \frac{1}{4} \, \beta \, \varepsilon \, c_f \int_0^1 \!\! \phi_i \, \phi_j' \! \left(\int_\xi^\xi \!\! \phi_k \, \phi_l \, \, d\xi \right) d\xi, \\ \eta_{ijkl} &= - \frac{1}{4} \frac{\beta^{3/2} \, \varepsilon \, c_f}{\mathcal{U}} \int_0^1 \!\! \phi_i \, \phi_j \, \phi_k \, \phi_l \, \, d\xi, \end{split}$$

$$\begin{split} \mu_{ijkl} &= - (1 - \beta) \int_0^1 \!\! \phi_i \, \phi_j'' \! \left(\int_\xi^1 \! \int_0^\xi \!\! \phi_k' \, \phi_l' \, d\xi \, d\xi \right) \! d\xi - \chi \, \beta \int_0^1 \!\! \phi_i \, \phi_j'' \! \left(\int_\xi^1 \!\! \phi_k' \, \phi_l \, d\xi \right) \! d\xi \\ &+ \! \left(1 + (\chi - 1)\beta \right) \! \int_0^1 \!\! \phi_i \, \phi_j' \! \left(\int_0^\xi \!\! \phi_k' \, \phi_l' \, d\xi \right) \! d\xi, \end{split}$$

$$r_{ijk} = \frac{1}{2} \mathcal{U}^{2} \varepsilon c_{d} \int_{0}^{1} \phi_{i} \phi_{j}' \left| \phi_{k}' \right| d\xi, \qquad \overline{s}_{ijk} = \frac{1}{2} \mathcal{U} \sqrt{\beta} \varepsilon c_{d} \int_{0}^{1} \phi_{i} \left| \phi_{j}' \right| \phi_{k} d\xi,$$

$$\widetilde{s}_{ijk} = \frac{1}{2} \mathcal{U} \sqrt{\beta} \varepsilon c_d \int_0^1 \phi_i \phi_j' |\phi_k| d\xi, \qquad t_{ijk} = \frac{1}{2} \beta \varepsilon c_d \int_0^1 \phi_i \phi_j |\phi_k| d\xi.$$

APPENDIX C: MATRIX AND TENSOR COEFFICIENTS FOR THE EXTENSIBLE CYLINDER FIXED AT BOTH ENDS

For the extensible cylinder fixed at both ends, the equation of motion in the *u*-direction is

$$\begin{split} M_{ij}^{u}\ddot{p}_{j} + K_{ij}^{u}p_{j} + A_{ijk}^{1}q_{j}q_{k} + A_{ijk}^{2}q_{j}\dot{q}_{k} + A_{ijk}^{3}\dot{q}_{j}\dot{q}_{k} + A_{ijk}^{4}q_{j}\ddot{q}_{k} + B_{ijkl}^{1}q_{j}q_{k} \big| q_{l} \big| + B_{ijkl}^{2}q_{j} \big| q_{k} \big| \dot{q}_{l} \\ + B_{iikl}^{3}q_{j}q_{k} \big| \dot{q}_{l} \big| + B_{iikl}^{4}q_{j}\dot{q}_{k} \big| \dot{q}_{l} \big| &= 0. \end{split}$$

The mass and stiffness matrices are defined by

$$M_{ij}^{u} = (1 - \beta) \int_{0}^{1} \psi_{i} \psi_{j} d\xi, \qquad K_{ij}^{u} = - \underset{0}{\text{Fe}} \int_{0}^{1} \psi_{i} \psi_{j}^{"} d\xi.$$

The coefficients A_{ijk}^1 , A_{ijk}^2 , A_{ijk}^3 , A_{ijk}^4 , B_{ijk}^1 , B_{ijk}^2 , B_{ijk}^3 , B_{ijk}^4 are computed numerically from the integrals of the eigenfunctions $\phi_i(\xi)$ and $\psi_i(\xi)$. They are defined by

$$\begin{split} A_{ijk}^1 &= -\chi \, \mathcal{U}^2 \int_0^1 \!\! \psi_i \, \phi_j'' \, \phi_k' \, \, d\xi - \int_0^1 \!\! \psi_i \, \phi_j'' \, \phi_k''' \, d\xi - \int_0^1 \!\! \psi_i \, \phi_j' \, \phi_k''' \, d\xi \\ & - \left(\frac{1}{2} \, \mathcal{U}^2 \varepsilon \, c_f (1+h) + (\gamma_C - \gamma_F) \right) \left(\frac{1}{2} \int_0^1 \!\! \psi_i \, \phi_j' \, \phi_k' \, \, d\xi - \int_0^1 \!\! (1-\xi) \, \psi_i \, \phi_j' \, \phi_k'' \, d\xi \right) \\ & + \left(\Gamma - \Pi_0 + \Pi \right) \int_0^1 \!\! \psi_i \, \phi_j' \, \phi_k'' \, \, d\xi + \delta \left(-\frac{1}{2} \left(\frac{1}{2} \, \mathcal{U}^2 \varepsilon \, c_f + \gamma_C \right) + \overline{\Gamma} - \Gamma \right) \int_0^1 \!\! \psi_i \, \phi_j' \, \phi_k'' \, d\xi, \\ A_{ijk}^2 &= -2 \, \chi \, \mathcal{U} \, \sqrt{\beta} \int_0^1 \!\! \psi_i \, \phi_j' \, \phi_k' \, \, d\xi, \\ A_{ijk}^3 &= \frac{1}{4} \, \beta \, \varepsilon \, c_f \int_0^1 \!\! \psi_i \, \phi_j' \, \phi_k \, \, d\xi, \\ A_{ijk}^4 &= -\chi \, \beta \int_0^1 \!\! \psi_i \, \phi_j' \, \phi_k \, \, d\xi, \\ B_{ijkl}^1 &= -\frac{1}{2} \, \mathcal{U}^2 \, \varepsilon \, c_d \int_0^1 \!\! \psi_i \, \phi_j' \, \phi_k' \, |\phi_i'| \, d\xi, \\ B_{ijkl}^3 &= -\frac{1}{2} \, \mathcal{U} \, \sqrt{\beta} \, \varepsilon \, c_d \int_0^1 \!\! \psi_i \, \phi_j' \, \phi_k' \, |\phi_l| \, d\xi, \\ B_{ijkl}^3 &= -\frac{1}{2} \, \mathcal{U} \, \sqrt{\beta} \, \varepsilon \, c_d \int_0^1 \!\! \psi_i \, \phi_j' \, \phi_k' \, |\phi_l| \, d\xi, \\ B_{ijkl}^4 &= -\frac{1}{2} \, \beta \, \varepsilon \, c_d \int_0^1 \!\! \psi_i \, \phi_j' \, \phi_k \, |\phi_l| \, d\xi. \end{split}$$

The equation of motion in the *v*-direction is

$$\begin{split} M_{ij}^{v}\ddot{q}_{j} + C_{ij}^{v}\dot{q}_{j} + K_{ij}^{v}q_{j} + D_{ijk}^{1}p_{j}q_{k} + D_{ijk}^{2}\dot{p}_{j}q_{k} + D_{ijk}^{3}p_{j}\dot{q}_{k} + D_{ijk}^{4}\dot{p}_{j}\dot{q}_{k} + D_{ijk}^{5}\ddot{p}_{j}q_{k} + E_{ijk}^{1}q_{j}\big|q_{k}\big| + E_{ijk}^{2}\big|q_{j}\big|\dot{q}_{k} \\ + E_{ijk}^{3}q_{j}\big|\dot{q}_{k}\big| + E_{ijk}^{4}\dot{q}_{j}\big|\dot{q}_{k}\big| + F_{ijkl}^{1}q_{j}q_{k}q_{l} + F_{ijkl}^{2}q_{j}q_{k}\dot{q}_{l} + F_{ijkl}^{3}q_{j}\dot{q}_{k}\dot{q}_{l} + F_{ijkl}^{4}\dot{q}_{j}\dot{q}_{k}\dot{q}_{l} + F_{ijkl}^{5}q_{j}q_{k}\ddot{q}_{l} = 0. \end{split}$$

The mass, damping and stiffness matrices in the v-direction are defined by

$$M_{ij}^{\nu} = (1 + (\chi - 1)\beta) \int_{0}^{1} \phi_{i} \phi_{j} d\xi,$$

$$C_{ij}^{\nu} = 2 \chi \mathcal{U} \sqrt{\beta} \int_{0}^{1} \phi_{i} \phi_{j}^{\prime} d\xi + \frac{1}{2} \mathcal{U} \varepsilon c_{f} \sqrt{\beta} \int_{0}^{1} \phi_{i} \phi_{j} d\xi,$$

The coefficients D^1_{ijk} , D^2_{ijk} , D^3_{ijk} , D^4_{ijk} , D^5_{ijk} , E^1_{ijk} , E^2_{ijk} , E^3_{ijk} , E^4_{ijk} , F^1_{ijkl} , F^2_{ijkl} , F^3_{ijkl} , F^4_{ijkl} , F^5_{ijkl} are computed numerically from the integrals of the eigenfunctions $\phi_i(\xi)$ and $\psi_i(\xi)$. They are defined by:

$$\begin{split} D^{1}_{ijk} &= -3 \int_{0}^{1} \phi_{i} \, \psi_{j}^{\prime \prime \prime} \phi_{k}^{\prime \prime} \, d\xi - 4 \int_{0}^{1} \phi_{i} \, \psi_{j}^{\prime \prime} \phi_{k}^{\prime \prime \prime} \, d\xi - 2 \int_{0}^{1} \phi_{i} \, \psi_{j}^{\prime} \, \phi_{k}^{\prime \prime \prime} \, d\xi - \int_{0}^{1} \phi_{i} \, \psi_{j}^{\prime \prime \prime} \phi_{k}^{\prime \prime} \, d\xi \\ &+ \left(\Gamma - \Pi_{o} + \delta \left(-\frac{1}{2} \left(\frac{1}{2} \mathcal{U}^{2} \varepsilon \, c_{f} + \gamma_{C} \right) + \overline{\Gamma} - \Gamma \right) \right) \left(\int_{0}^{1} \phi_{i} \, \psi_{j}^{\prime} \, \phi_{k}^{\prime \prime} \, d\xi + \int_{0}^{1} \phi_{i} \, \psi_{j}^{\prime \prime} \, \phi_{k}^{\prime} \, d\xi \right) \\ &+ \left(\Pi - 2 \, \chi \, \mathcal{U}^{2} \right) \left(2 \, \int_{0}^{1} \phi_{i} \, \psi_{j}^{\prime} \, \phi_{k}^{\prime \prime} \, d\xi + \int_{0}^{1} \phi_{i} \, \psi_{j}^{\prime \prime} \, \phi_{k}^{\prime} \, d\xi \right) \\ &- \left(\frac{1}{2} \, \mathcal{U}^{2} \varepsilon \, c_{f} (1 + 2 \, h) + \left(\gamma_{C} - 2 \, \gamma_{F} \right) \right) \left(\int_{0}^{1} \phi_{i} \, \psi_{j}^{\prime} \, \phi_{k}^{\prime} \, d\xi - \int_{0}^{1} (1 - \xi) \phi_{i} \, \psi_{j}^{\prime} \, \phi_{k}^{\prime \prime} \, d\xi \right) \\ &+ \left(\frac{1}{2} \, \mathcal{U}^{2} \varepsilon \, c_{f} (1 + h) + \left(\gamma_{C} - \gamma_{F} \right) \right) \int_{0}^{1} (1 - \xi) \phi_{i} \, \psi_{j}^{\prime \prime} \, \phi_{k}^{\prime} \, d\xi, \end{split}$$

$$D^{2}_{ijk} = -\chi \, \mathcal{U} \, \sqrt{\beta} \left(3 \, \int_{0}^{1} \phi_{i} \, \psi_{j}^{\prime} \, \phi_{k}^{\prime} \, d\xi + 2 \, \int_{0}^{1} \phi_{i} \, \psi_{j} \, \phi_{k}^{\prime \prime} \, d\xi \right),$$

$$D_{ijk}^{3} = -4 \chi \mathcal{U} \sqrt{\beta} \int_{0}^{1} \phi_{i} \psi_{j}' \phi_{k}' d\xi + \frac{1}{2} \mathcal{U} \sqrt{\beta} \varepsilon c_{f} \int_{0}^{1} \phi_{i} \psi_{j}' \phi_{k} d\xi,$$

$$D_{ijk}^{4} = -2 \chi \beta \int_{0}^{1} \phi_{i} \psi_{j} \phi'_{k} d\xi + \frac{1}{2} \beta \varepsilon c_{f} \int_{0}^{1} \phi_{i} \psi_{j} \phi_{k} d\xi,$$

$$D_{ijk}^5 = -\chi \beta \int_0^1 \phi_i \psi_j \phi_k' d\xi,$$

$$E_{ijk}^{1} = \frac{1}{2} \mathcal{U}^{2} \varepsilon c_{d} \int_{0}^{1} \phi_{i} \phi'_{j} \left| \phi'_{k} \right| d\xi,$$

$$E_{ijk}^{3} = \frac{1}{2} \mathcal{U} \sqrt{\beta} \varepsilon c_{d} \int_{0}^{1} \phi_{i} \phi'_{j} |\phi_{k}| d\xi,$$

$$E_{ijk}^2 = \frac{1}{2} \mathcal{U} \sqrt{\beta} \varepsilon c_d \int_0^1 \!\! \phi_i \left| \phi_j' \right| \phi_k \ d\xi,$$

$$E_{ijk}^{4}=rac{1}{2}oldsymbol{arepsilon}\,oldsymbol{arepsilon}_{d}oldsymbol{\phi}_{i}\,oldsymbol{\phi}_{i}\,igg|oldsymbol{\phi}_{k}igg|\,d\xi,$$

$$F_{ijkl}^{2} = -\chi \, \mathrm{U} \sqrt{\beta} \left(\frac{7}{2} \, \int_{0}^{1} \! \phi_{i} \, \phi_{j}' \, \phi_{k}' \, \phi_{l}' \, d\xi + \frac{3}{2} \, \int_{0}^{1} \! \phi_{i} \, \phi_{j}' \, \phi_{k}'' \, \phi_{l} \, d\xi \right),$$

$$F_{ijkl}^{3} = -\frac{3}{2} \chi \beta \int_{0}^{1} \phi_{i} \phi'_{j} \phi_{k} \phi'_{l} d\xi,$$

$$F_{ijkl}^{4} = -\frac{1}{4} \frac{\beta^{3/2} \varepsilon c_f}{\mathcal{U}} \int_0^1 \phi_i \phi_j \phi_k \phi_l d\xi,$$

$$F_{ijkl}^5 = -\chi \beta \int_0^1 \phi_i \, \phi'_j \, \phi'_k \, \phi_l \, d\xi.$$

APPENDIX D: MATRIX AND TENSOR COEFFICIENTS FOR THE EXTENSIBLE CANTILEVERED CYLINDER TERMINATED IN A TAPERING FREE-END

When the cantilevered cylinder is considered to be extensible and terminated by a tapering freeend, we shall define the mass, damping and stiffness matrices in the *v*-direction as follows

$$\begin{split} M_{ij}^{\nu} &= \left(1 + (\chi f - 1)\beta\right)\chi_{e} \,\phi_{i}(1)\phi_{j}(1) + \left(1 + (\chi - 1)\beta\right)\int_{0}^{1}\!\!\!\phi_{i} \,\phi_{j} \,d\xi, \\ C_{ij}^{\nu} &= \left(\frac{1}{2}\,\overline{\chi}_{e}\,\varepsilon\,c_{f} - \chi\,f\right)\mathcal{U}\,\sqrt{\beta}\,\phi_{i}(1)\phi_{j}(1) + \chi\,f\,\mathcal{U}\,\sqrt{\beta}\,\chi_{e}\,\phi_{i}(1)\phi_{j}'(1) + \\ &\quad 2\,\chi\,\mathcal{U}\,\sqrt{\beta}\int_{0}^{1}\!\!\!\phi_{i}\,\phi_{j}' \,d\xi + \frac{1}{2}\,\mathcal{U}\,\varepsilon\,c_{f}\sqrt{\beta}\int_{0}^{1}\!\!\!\phi_{i}\,\phi_{j} \,d\xi, \\ K_{ij}^{\nu} &= \left((\gamma_{C} - \chi\gamma_{F})\chi_{e} + \frac{1}{2}\,\mathcal{U}^{2}\varepsilon\,c_{f}(\overline{\chi}_{e} + h\,\chi_{e}) - \chi\,f\,\mathcal{U}^{2}\right)\phi_{i}(1)\,\phi_{j}'(1) + \chi\,\mathcal{U}^{2}\int_{0}^{1}\!\!\!\phi_{i}\,\phi_{j}'' \,d\xi \\ &\quad + \left(\frac{1}{2}\,\mathcal{U}^{2}\varepsilon\,c_{f}(1 + h) + (\gamma_{C} - \gamma_{F})\right)\left(\int_{0}^{1}\!\!\!\phi_{i}\,\phi_{j}' \,d\xi - \int_{0}^{1}\!\!\!\left(1 - \xi\right)\!\!\!\phi_{i}\,\phi_{j}'' \,d\xi\right) + \int_{0}^{1}\!\!\!\phi_{i}\,\phi_{j}''' \,d\xi \\ &\quad - (\Gamma + \Pi)\int_{0}^{1}\!\!\!\phi_{i}\,\phi_{j}'' \,d\xi - \delta\left(-\frac{1}{2}\left(\frac{1}{2}\,\mathcal{U}^{2}\varepsilon\,c_{f} + \gamma_{C}\right) + \overline{\Gamma} - \Gamma\right)\int_{0}^{1}\!\!\!\phi_{i}\,\phi_{j}'' \,d\xi. \end{split}$$

Actually, the mass and stiffness matrices in the *u*-direction remain as defined in Appendix C.

APPENDIX E: ALTERNATIVE FORM OF MATRIX COEFFICIENTS FOR CANTILEVERED CYLINDER

Introducing the normal and tangential viscous parameters in the equation of motion of the inextensible cantilevered cylinder, εc_N and εc_T respectively, the mass, damping and stiffness matrices are then defined as follows

$$\begin{split} M_{ij} &= \left(1 + \left(\chi f - 1\right)\beta\right)\chi_{e}\,\phi_{i}\left(1\right)\phi_{j}\left(1\right) + \left(1 + \left(\chi - 1\right)\beta\right)\delta_{ij}\,,\\ C_{ij} &= \left(\frac{1}{2}\,\overline{\chi}_{e}\,\varepsilon\,c_{N} - \chi\,f\right)\mathcal{U}\,\sqrt{\beta}\,\phi_{i}\left(1\right)\phi_{j}\left(1\right) + \chi\,f\,\mathcal{U}\,\sqrt{\beta}\,\chi_{e}\,\phi_{i}\left(1\right)\phi_{j}'\left(1\right) + 2\,\chi\,\mathcal{U}\,\sqrt{\beta}\,b_{ij} + \frac{1}{2}\,\mathcal{U}\,\varepsilon\,c_{N}\,\sqrt{\beta}\,\delta_{ij}\,,\\ K_{ij} &= \left(\left(\gamma_{C} - \gamma_{F}\right)\chi_{e} + \frac{1}{2}\,\mathcal{U}^{2}\left(\varepsilon\,c_{N}\,\overline{\chi}_{e} + \varepsilon\,c_{T}\,h\,\chi_{e}\right) - \chi\,f\,\mathcal{U}^{2}\right)\phi_{i}\left(1\right)\phi_{j}'\left(1\right) + \chi\,\mathcal{U}^{2}c_{ij} + \\ \left(\gamma_{C} - \gamma_{F} + \frac{1}{2}\,\mathcal{U}^{2}\varepsilon\,c_{T}\,h\right)\left(b_{ij} + d_{ij} - c_{ij}\right) + \frac{1}{2}\,\mathcal{U}^{2}\varepsilon\,c_{T}\left(d_{ij} - c_{ij}\right) + \frac{1}{2}\,\mathcal{U}^{2}\varepsilon\,c_{N}\,b_{ij} + \lambda_{j}^{4}\delta_{ij} - \frac{1}{2}\,\mathcal{U}^{2}c_{b}\,c_{ij}\,; \end{split}$$

 δ_{ij} is Kronecker's delta, λ_j are the dimensionless eigenvalues of a cantilever beam and the constants, b_{ij} , c_{ij} , d_{ij} are defined in Appendix B.